

1 **Live imaging of SARS-CoV-2 infection in mice reveals neutralizing antibodies require Fc
2 function for optimal efficacy**

3
4 Irfan Ullah^{1,#}, Jérémie Prévost^{2,3,#}, Mark S Ladinsky^{4,@}, Helen Stone^{5,@}, Maolin Lu^{5,@}, Sai Priya
5 Anand^{2,6}, Guillaume Beaudoin-Bussières^{2,3}, Mehdi Benlarbi², Shilei Ding², Romain Gasser^{2,3},
6 Corby Fink⁷, Yaozong Chen⁸, Alexandra Tauzin^{2,3}, Guillaume Goyette², Catherine Bourassa²,
7 Halima Medjahed², Matthias Mack⁹, Kunho Chung¹, Craig B Wilen¹⁰, Gregory A. Dekaban^{7,13},
8 Jimmy D. Dikeakos⁷, Emily A. Bruce¹¹, Daniel E Kaufmann^{2,3}, Leonidas Stamatatos^{12,14}, Andrew
9 T. McGuire^{12,14,15}, Jonathan Richard^{2,3}, Marzena Pazgier⁸, Pamela J.
10 Bjorkman⁴, Walther Mothes^{5,*}, Andrés Finzi^{2,3,6,*}, Priti Kumar^{1,*} and Pradeep D. Uchil^{5,*,\$}

11

12 ¹Department of Internal Medicine, Section of Infectious Diseases, Yale University School of
13 Medicine, New Haven, CT 06520

14 ²Centre de Recherche du CHUM, Montreal, QC, Canada, H2X0A9

15 ³Département de Microbiologie, Infectiologie et Immunologie, Université de Montréal, Montreal,
16 QC, Canada, H2X0A9

17 ⁴Division of Biology and Biological Engineering, California Institute of Technology, Pasadena,
18 CA 91125

19 ⁵Department of Microbial Pathogenesis, Yale University School of Medicine, New Haven CT
20 06510

21 ⁶Department of Microbiology and Immunology, McGill University, Montreal, Qc, Canada

22 ⁷Department of Microbiology and Immunology, University of Western Ontario, London, ON,
23 Canada N6A 5B7

24 ⁸Infectious Disease Division, Department of Medicine, Uniformed Services University of the
25 Health Sciences, Bethesda, MD 20814-4712, USA

26 ⁹Universitätsklinikum Regensburg, Innere Medizin II – Nephrologie, 93042 Regensburg,
27 Germany
28 ¹⁰Departments of Laboratory Medicine and Immunobiology, Yale University School of Medicine,
29 New Haven, CT, 06520
30 ¹¹Division of Immunobiology, Dept. of Medicine, Larner College of Medicine, University of
31 Vermont. Burlington, VT. 05405. USA.
32 ¹²Vaccine and Infectious Disease Division, Fred Hutchinson Center, Seattle, WA
33 ¹³Molecular Medicine Research Laboratories, Robarts Research Institute, University of Western
34 Ontario, London, ON, Canada N6A 5B7
35 ¹⁴Department of Global Health, University of Washington, Seattle, WA
36 ¹⁵Department of Laboratory Medicine and Pathology, University of Washington, Seattle, WA
37 # , @ Contributed equally to the work
38 ***Address of correspondence to:**
39 \$pradeep.uchil@yale.edu, priti.kumar@yale.edu, andres.finzi@umontreal.ca, ~~walther.mothes@~~
40 yale.edu
41 \$Lead Author
42
43 **Figures: 7**
44 **Supplemental figures: 7**
45 **Supplemental videos: 4**

46 **SUMMARY**

47 Neutralizing antibodies (Nabs) are effective in treating COVID-19 but the mechanism of immune
48 protection is not fully understood. Here, we applied live bioluminescence imaging (BLI) to monitor
49 the real-time effects of NAb treatment in prophylaxis and therapy of K18-hACE2 mice intranasally
50 infected with SARS-CoV-2-nanoluciferase. We visualized sequential spread of virus from the
51 nasal cavity to the lungs followed by systemic spread to various organs including the brain,
52 culminating in death. Highly potent Nabs from a COVID-19 convalescent subject prevented, and
53 also effectively resolved, established infection when administered within three days of infection.
54 In addition to direct neutralization, *in vivo* efficacy required Fc effector functions of Nabs, with
55 contributions from monocytes, neutrophils and natural killer cells, to dampen inflammatory
56 responses and limit immunopathology. Thus, our study highlights the requirement of both Fab
57 and Fc effector functions for an optimal *in vivo* efficacy afforded by Nabs against SARS-CoV-2.

58

59 **Key words:** SARS-CoV-2, COVID-19, nanoluciferase, bioluminescence imaging, neutralizing
60 antibodies, convalescent patients, human ACE2 transgenic mice, monocytes, natural killer cells,
61 monocytes, pathogenesis, inflammatory cytokines, Fc effector functions

62 **Introduction**

63 SARS-CoV-2-neutralizing monoclonal antibodies (NAbs) are an attractive countermeasure for
64 both COVID-19 prevention and therapy (Schafer et al., 2021; Voss et al., 2020; Weinreich et al.,
65 2021). To date, multiple NAbs against the spike (S) glycoprotein of SARS-CoV-2 have been
66 identified from convalescent subjects. The majority of NAbs bind to the receptor binding domain
67 (RBD) in the S1 subunit for inhibiting virus attachment to the human Angiotensin Converting
68 Enzyme 2 (hACE2) receptor. NAbs against the N-terminal domain (NTD) of S1 as well as the S2
69 subunit have also been isolated (Anand et al., 2021b; Liu et al., 2020; Voss et al., 2020). NAbs
70 have demonstrated varying levels of efficacy and protection in multiple animal models of SARS-
71 CoV-2 (Alsoussi et al., 2020; Baum et al., 2020; Fagre et al., 2020; Hansen et al., 2020; Hassan
72 et al., 2020; Li et al., 2020; Rogers et al., 2020; Shi et al., 2020b; Winkler et al., 2020; Zost et al.,
73 2020a; Zost et al., 2020b). However, the *in vitro* neutralization potency of NAbs has not
74 consistently correlated with *in vivo* protection (Bournazos et al., 2014; Schafer et al., 2021). While
75 the antigen binding domain (Fab) of antibodies are critical for neutralization, the fragment
76 crystallizable (Fc) domain can contribute significantly to their *in vivo* efficacy (Bournazos et al.,
77 2019; Bournazos et al., 2014; DiLillo et al., 2014). Fc engagement of Fc gamma receptors (FcγRs)
78 can elicit complement-dependent cytotoxicity (CDC), antibody-dependent cellular cytotoxicity
79 (ADCC) and antibody-dependent cellular phagocytosis (ADCP). The Fc region can recruit natural
80 killer (NK) cells, monocytes, or neutrophils that can facilitate clearance of infected cells and shape
81 the cytokine response produced by these cells for enhancing adaptive and cell-mediated immune
82 responses (Lu et al., 2018). Fc effector functions can also be detrimental to the host, especially
83 against respiratory diseases such as respiratory syncytial virus (RSV) and SARS-CoV-1 leading
84 to antibody-dependent enhancement (ADE) and aggravated disease pathology (Bolles et al.,
85 2011; Halstead and Katzelnick, 2020; Ruckwardt et al., 2019). Therefore, a careful investigation

86 NAb mechanisms that elicit protective or pathological consequences is required before their
87 clinical deployment.

88 Animal models evaluated to date (Johansen et al., 2020; Leist et al., 2020a; Leist et al.,
89 2020b) have not fully recapitulated pathological features of human COVID-19. Transgenic mice
90 expressing hACE2 under the cytokeratin 18 promoter (K18-hACE2 mice) however, have some
91 distinct advantages. Primarily, they are permissive and highly susceptible to human-tropic SARS-
92 CoV-2 virus strains and succumb to infection within a week (McCray et al., 2007; Shi et al., 2020a;
93 Winkler et al., 2020). This allows for a rapid turnaround and a high bar for identifying effective
94 prophylactic or therapeutic intervention strategies. In susceptible humans, SARS-CoV-2 infection
95 disables innate immunity and elicits an imbalanced inflammatory cytokine response in the lungs
96 leading to acute respiratory distress syndrome (ARDS) which is the major cause of death
97 (Graham and Baric, 2020). Lethality in K18-hACE2 mice was initially associated with lung
98 inflammation, cytokine storm and impaired respiratory function (Winkler et al., 2020). However, it
99 has recently been recognized that the pathogenic endpoint in K18-hACE2 mice is a result of viral
100 neuroinvasion and an ensuing neuronal disease (Carossino et al., 2021; Golden et al., 2020; Leist
101 et al., 2020a). Infact, many patients display a myriad of neurological symptoms during and after
102 recovery from SARS-CoV-2 infection (Ellul et al., 2020). Finally, mouse Fc_γR_s display similar
103 affinities to human antibodies (Dekkers et al., 2017). Therefore, K18-hACE2 mice serve as
104 excellent models for evaluating and screening candidate human NAbS for their effects on SARS-
105 CoV-2 replication and pathogenesis.

106 Bioluminescence imaging (BLI)-guided studies permit live visualization of pathogen
107 spread to diverse anatomical site, the identification of relevant tissues of interest and a real-time
108 readout of treatment regimens accelerating the evaluation process. A BLI-driven platform has not
109 been harnessed for studying infectious respiratory pathogens like SARS-CoV-2 that require level
110 3 biosafety containment. Here, we have established a BLI-driven approach to study SARS-CoV-
111 2 infection with a well characterized replication competent virus carrying a nanoluciferase (nLuc)

112 reporter in the place of the Orf7A gene (Xie et al., 2020a; Xie et al., 2020b). SARS-CoV-2-nLuc
113 closely mimics the wildtype virus replication kinetics and stably maintains the nLuc reporter over
114 five generations *in vitro*. In addition, Orf7a deletion was recently shown to induce comparable
115 pathology to the wild-type virus (Silvas et al., 2021). Our *in vivo* imaging studies revealed that the
116 virus spreads from the nasal cavity to lungs for establishing infection. This was followed by
117 infection of cervical lymph nodes (cLN_s), brain, and systemic dissemination. Once neuroinvasion
118 occurred, the virus replicated rapidly in the brain leading to fulminant infection and death by 6-7
119 days post infection (dpi). A single prophylactic intraperitoneal (i.p.) administration of highly potent
120 NAbs isolated from a convalescent COVID-19 subject completely prevented SARS-CoV-2
121 infection and mortality in K18-hACE2 mice. Protection was associated with widespread
122 localization of administered NAb_s and Fc-mediated effector functions with contributions from
123 monocytes and NK cells as well as reduced induction of inflammatory cytokines. BLI also revealed
124 a therapeutic window of 3 dpi for NAb for successfully halting progression of established infection
125 in the lungs as well as to distal tissues. Thus, our BLI-driven study highlighted the requirement for
126 both neutralizing and Fc effector functions of NAb_s to elicit optimal virological and immunological
127 outcome against SARS-CoV-2.

128

129 **Results**

130 **BLI allows Visualization of SARS-CoV-2 Replication Dynamics and Pathogenesis**

131 We tracked spread of SARS-CoV-2-nLuc using BLI after intranasal (i.n.) challenge in K18-hACE2
132 mice (**Figure 1A**). 1×10^5 FFU of SARS-CoV-2 generated sufficient photon flux to allow non-
133 invasive BLI. Importantly, luciferase signal was absent in C57BL/6J (B6) mice lacking hACE2
134 (**Figure 1B**). Temporal tracking of emitted light intensities revealed that the virus replicated in the
135 nasal cavity in a biphasic manner (**Figure 1C**). Luminescent signal in the nose increased in the
136 first two days of infection after which it diminished before increasing again between 5 to 6 dpi

137 when systemic spread occurred. The first signs of infection in the lungs were observed at 1 dpi.
138 The nLuc signal then steadily increased in the lungs until 3 dpi and plateaued thereafter. We
139 detected nLuc signals in the cLN_s and brain region (imaging in ventral position) at 4 dpi. There
140 was a steep rise in nLuc activity in the brain from 4 to 6 dpi indicating neuroinvasion and robust
141 virus replication (**Figure 1B, C, Video S1**). This was accompanied by widespread replication of
142 the virus in the gut and genital tract with concomitant loss in body weight. By 6 dpi, the infected
143 K18-hACE2 mice lost 20% of their initial body weight, became moribund and succumbed to the
144 infection (**Figure 1D, E**). In contrast, as expected, B6 mice did not experience any weight loss
145 and survived the virus challenge.

146 To visualize the extent of viral spread with enhanced sensitivity and resolution, we imaged
147 individual organs after necropsy (**Figure 1B, F**). nLuc signal was absent in B6 mice while most
148 organs analyzed from K18-hACE2 mice showed nLuc activity with maximum signal detected in
149 the brain followed by the lung and nasal cavity (**Figure 1F**). These observations mirrored viral
150 loads [Focus Forming Units (FFUs) and nLuc activity] in the brain, lung and nasal cavity (**Figure**
151 **1G, H**). Real-time PCR analyses to detect N gene mRNA as well as histological analyses of
152 organs confirmed widespread infection (**Figure S1A, B**).

153 Reporter-expressing viruses often purge foreign genes, particularly *in vivo*, due to fitness
154 and immune pressure (Falzarano et al., 2014; Ventura et al., 2019). To estimate the stability of
155 nLuc reporter, we compared the copy numbers of SARS-CoV-2 nucleocapsid (N) to nLuc in the
156 viral RNA by real-time PCR analyses of input virions and virions isolated from sera of mice at 6
157 dpi. The ratio of copy numbers between the two samples sets did not change significantly (**Figure**
158 **1I**) indicating that the reporter was stable throughout the experimental timeline. Thus, nLuc activity
159 was an excellent surrogate to follow virus replication *in vivo*.

160 SARS-CoV-2 infection triggers an imbalanced immune response and a cytokine storm
161 that contributes significantly to pathogenesis (Del Valle et al., 2020). We compared the mRNA
162 levels of inflammatory cytokines IL6, CCL2, CXCL10 and IFN γ in the lungs and brains of mice

163 after necropsy at 6 dpi. Indeed, most cytokines mRNAs were significantly upregulated in both
164 organs of infected K18-hACE2 mice compared to B6 (**Figure 1J, K**). Overall, cytokine mRNAs
165 were higher in the brain compared to lungs with CXCL10 mRNA copy numbers reaching ~1000
166 fold higher in K18-hACE2 than in B6 mice corroborating extensive infection (**Figure 1J, K**).

167 We next used BLI to illuminate areas of infected regions within lungs, brain, and testis for
168 directed histology and electron tomographic studies (**Figure 2**). Higher resolution imaging
169 revealed that SARS-CoV-2 virions were associated to large extent with capillary endothelial cell
170 and/or alveolar type-1 cells in the lungs (**Figure 2A-D; Video S2**). In the brain, neuronal cells
171 (MAP2⁺GFAP⁻CD68⁻CD11b⁻) were positive for SARS-CoV-2 N and EM tomography revealed an
172 array of SARS-CoV-2 virions associated within the dendrites (**Figure 2E-J, Figure S1C, Video**
173 **S3**). In the testis, Sertoli cells stained positively for N (**Figure 2K-N, Video S4**). EM tomography
174 also showed a large population of virions within pleomorphic membrane-bound compartments of
175 Sertoli cells.

176

177 **Highly Potent SARS-CoV-2 NAbs CV3-1 and CV3-25 from a Convalescent Donor**

178 We recently reported and characterized plasma from a COVID-19 convalescent subject
179 (S006) with potent neutralizing activity and high levels of SARS-CoV-1 cross-reactive Abs (Lu et
180 al., 2020). We probed the B cell receptor (BCR) repertoire from this donor to isolate broad and
181 potent NAbs. Using a recombinant SARS-CoV-2 S ectodomain (S2P) as a bait to identify antigen-
182 specific B cells, we collected and screened a library of S-targeted BCR clones and identified two
183 most potent NAb candidates: CV3-1 and CV3-25. We first characterized their epitope specificity
184 using ELISA, cell-surface staining, virus capture assay and surface plasmon resonance (SPR)
185 (Ding et al., 2020; Prevost et al., 2020). Both NAbs recognized SARS-CoV-2 S efficiently with a
186 low-nanomolar affinity, as a stabilized ectodomain (S-6P) or when displayed on cells and virions
187 (**Figure 3A-E**). While CV3-1 bound the SARS-CoV-2 RBD, CV3-25 targeted the S2 subunit

188 (**Figure 3A, D-E**) and cross-reacted with SARS-CoV-1 S on cells or virions, but not with S from
189 other human *Coronaviruses* (**Figure 3B-C**). In agreement with the previous smFRET data for
190 S006 plasma, CV3-1 stabilized S in the RBD-up (~0.1 FRET) conformation (**Figure 3F-H**), as
191 seen with hACE2 and most RBD-directed NAbs (Lu et al., 2020). Interestingly, CV3-25-bound S
192 showed a partial shift towards downstream conformations (~0.1 and ~0.3 FRET), suggesting a
193 distinct inhibitory mechanism from CV3-1 (**Figure 3F-H**).

194 We next measured the ability of CV3-1 and CV3-25 to neutralize and mediate Fc-
195 dependent antibody functions. While both NAbs blocked infection by SARS-CoV-
196 2 pseudovirus or live virus and interfered with S-driven cell-to-cell fusion, CV3-1 was ~10 times
197 more potent than CV3-25 (**Figure 3I-L**). To evaluate Fc-mediated effector functions of the NAbs,
198 we used assays that quantify the ADCC and ADCP activities against S-expressing cells. CV3-1
199 and CV3-25 efficiently bound and eliminated S-expressing cells by stimulating cytotoxic and
200 phagocytic responses in immune effector cells (**Figure 3L-N**). Overall, both NAbs displayed
201 significant neutralization and Fc-dependent antibody functions, although CV3-1 was found to be
202 more effective for most of the assessed functions. The combination of the two NAbs (1:1 ratio)
203 was found to be phenotypically similar to the responses seen with CV3-1 alone (**Figure 3I-N**).

204

205 **Prophylactic Treatment with NAbs Protects K18-hACE2 Mice from SARS-CoV-2 Infection**

206 We first monitored the biodistribution of Alexa Fluor (AF) conjugated CV3-1 and CV3-25 in various
207 tissues 24 h after i.p. delivery in mice by fluorescence imaging, histology and ELISA. All three
208 approaches revealed widespread distribution of the NAbs to multiple organs and target tissues
209 including the nasal cavity, lung and the brain (**Figure S2, S3A-D**). Next, we tested a prophylactic
210 regimen where each NAb was delivered i.p. alone (12.5 mg/kg body weight) or in 1:1 combination
211 (6.25 mg each NAb/kg body weight) 24 h before i.n. challenge with SARS-CoV-2 nLuc (**Figure**
212 **4A**). Temporal monitoring by whole-body BLI revealed that all three prophylactic regimens

213 substantially reduced SARS-CoV-2 infection in the lungs and subsequent spread (**Figure 4B-D**).
214 Remarkably, pretreatment with CV3-1 alone or in combination with CV3-25 (cocktail 1:1)
215 produced near complete protection from SARS-CoV-2 infection with no signals detected in
216 multiple organs after non-invasive imaging or after terminal necropsy at 22 dpi (**Figure 4B-D, G,**
217 **H**). Moreover, all test cohorts survived with no discernible weight loss, nLuc activity or viral loads
218 in all organs tested signifying complete control of virus infection (**Figure 4E-I**). Lung and
219 subsequent neuroinvasion did occur, albeit at reduced intensity, in CV3-25-pretreated animals
220 which was corroborated by imaging of individual organs after necropsy (**Figure 4B, G, H**). CV3-
221 25 delayed mortality by ~2 days in 4 out of the 6 animals and viral loads in the nasal cavity, lungs,
222 and brain at the time of necropsy (8 dpi) were similar to that in the control cohorts treated with
223 isotype-matched antibodies at 6 dpi (**Figure 4F, I**).

224 CV3-1 or NAb cocktail pre-treatment also prevented the inflammatory cytokine induction
225 seen in control and CV3-25 pre-treated cohorts (**Figure 4J, K**). In contrast, heightened levels of
226 cytokine mRNA were detected in mice that had succumbed to infection and the control cohort
227 (**Figure 4J, K**). Mice that survived in the CV3-25 pretreated cohorts, regained body weight and at
228 22 dpi, had no detectable virus in organs and exhibited base-line inflammatory cytokine induction
229 (**Figure 4E-K**). Overall, our data indicated that CV3-1 alone, or in combination with CV3-25,
230 inhibited establishment of virus infection and fully protected K18-hACE2 mice. Histology of brain
231 tissue revealed that NAbs CV3-1 and CV3-25 persisted even at 6 dpi (**Figure S3E**). Consistent
232 with virus infection in the brain, CV3-25 localized heavily to the surface of infected neurons at 6
233 dpi, in addition to endothelial cells, which was predominantly observed before infection. In
234 contrast, CV3-1 localization remained unaltered due to the absence of viral neuroinvasion in this
235 cohort (**Figure S3E**). In addition, *in vivo* dose response studies revealed that as little as 0.75 mg
236 CV3-1/kg body weight protected 50% of the treated cohort from lethal SARS-CoV-2 infection
237 (**Figure S4**). These data indicated that CV3-1 is highly potent at halting SARS-CoV-2 infection
238 and contributed to protection observed in the cohort treated with the cocktail.

239 **CV3-1 Therapy Rescues Mice from Lethal SARS-CoV-2 Infection**

240 CV3-1 NAb alone completely protected K18-hACE2 mice against SARS-CoV-2-induced mortality.
241 We therefore explored if CV3-1 could also cure infected mice. Mice infected with SARS-CoV-2-
242 nLuc were administered CV3-1 at 1, 3, and 4 dpi after confirming SARS-CoV-2 infection was
243 established in the lungs of all mice (**Figure 5A**). Temporal imaging and quantification of nLuc
244 signal revealed that CV3-1, when administered at 1 and 3 dpi, controlled virus spread and
245 successfully prevented neuroinvasion (**Figure 5B-D, G, H**). This was corroborated by no weight
246 loss and/or recuperation of body weight, undetectable viral loads as well as near-baseline levels
247 of inflammatory cytokines in tissues (**Figure 5E-K**). CV3-1 therapy at 4 dpi, however, could neither
248 control virus spread nor neuroinvasion resulting in death of 75% of the mice in this cohort (**Figure**
249 **5B-F**) with loss in body weight, high levels of inflammatory cytokines and tissue viral loads, similar
250 to that in the control cohort (**Figure 5E-K**). Thus, the therapeutic window of maximal efficacy for
251 CV3-1 treatment extends for up to 3 days from the initiation of SARS-CoV-2 infection to
252 successfully prevent lethality.

253

254 **CV3-1 and CV3-25 Require Antibody Effector Functions For *in vivo* efficacy**

255 Highly potent antibodies can effectively neutralize free viruses and may also mediate Fc-
256 recruitment of immune cells to eliminate infected cells. We therefore explored a role for Fc-
257 mediated effector functions in protection *in vivo*. We generated Leucine to Alanine (L234A/L235A,
258 LALA) mutant versions of both NAbs to impair interaction with Fc receptors (Saunders, 2019).
259 Our *in vitro* assays confirmed that, while ADCC and ADCP activities were compromised, LALA
260 mutations had no impact on S binding and neutralizing capacities of both NAbs (**Figure S5**).
261 Biodistribution analyses of AF647-conjugated CV3-1 and CV3-25 LALA NAbs, 24h after i.p.
262 administration indicated penetration into most tissues (**Figure S5**).

263 We next tested the impact of LALA mutations on the prophylactic efficacy of CV3-1 and
264 CV3-25 (**Figure S6A**). Longitudinal non-invasive BLI and terminal imaging analyses after

265 necropsy, body weight changes, survival and viral load estimations revealed that LALA mutations
266 had indeed compromised the protective efficacy of both antibodies (**Figure S6A-I**). SARS-CoV-2
267 replicated better, invaded the brain and induce body weight loss in cohorts treated with LALA
268 NAbs compared to the corresponding wild-type NAbs (**Figure S6D-E**). Histology at 6 dpi revealed
269 that both LALA NAbs had penetrated the brain tissue during the course of infection and bound
270 the surface of infected neurons (**Figure S5G, H**). While CV3-1-treated animals had no detectable
271 viral loads at 6 dpi, CV3-1 LALA pretreated mice had higher tissue viral loads indicating
272 compromised protective efficacy (**Figure S6I**). Similarly, while tissue viral loads in CV3-25 treated
273 mice were reduced by a log, those in CV3-25 LALA treated mice were comparable to that in
274 control cohorts. Moreover, the delayed mortality and 25% protective efficacy offered by CV3-25
275 was abrogated and the ability of CV3-1 to provide 100% protection from SARS-CoV-2-induced
276 mortality was reduced to 62.5% with the corresponding LALA mutants (**Figure S6F**). Additionally,
277 there was an overall increase in the signature inflammatory cytokine profile in mice pre-treated
278 with LALA NAbs (**Figure S6J, K**).

279 The requirement for Fc effector function during CV3-1 prophylaxis was surprising as we
280 did not detect infection in CV3-1 treated mice both by non-invasive and post-necropsy tissue
281 imaging at 6 dpi (**Figure 4**). However, examination of tissues at 3 dpi did reveal weak nLuc signals
282 in the nasal cavity and lungs despite absence of signal by non-invasive imaging (**Figure S5J-M**).
283 PCR analyses also confirmed the presence SARS-CoV-2 N RNA in these tissues at 3 dpi (**Figure**
284 **S5N**). The data indicated that some of the incoming virions did not encounter CV3-1 and managed
285 to establish infection during prophylaxis and hence Fc effector functions were required to
286 eliminate them.

287 Our data thus implied that immune cell components would be critical during CV3-1 therapy
288 (**Figure 6A**). Indeed, while CV3-1 treatment at 3 dpi controlled infection, cohorts treated with CV3-
289 1 LALA displayed rapidly spreading lung infection and fully succumbed by 6 dpi after an
290 accelerated loss in body weight (**Figure 6B-F**). High viral loads and cytokine levels in nose, lung,

291 and brain also reflected the failure of the LALA NAbs to treat pre-established viral infection (**Figure**
292 **6G**). Notably, while the lung viral loads in CV3-1 LALA NAb-treated cohort were similar to that in
293 the control, inflammatory cytokine mRNA levels in lungs, *CXCL10* in particular, were significantly
294 higher suggesting a crucial requirement for Fc-engagement in curbing a cytokine-storm like
295 phenotype (**Figure 6H-I**).

296

297 **Monocytes and NK cells Contribute to Antibody-mediated Effector Functions *In Vivo***

298 To identify the immune cell types engaged by NAbs, we initiated NK cell depletion (α -NK1.1) prior
299 to CV3-1 prophylaxis. Flow cytometric analyses confirmed NK cell depletion in α -NK1.1 treated
300 cohorts. (**Figure S7J, K**). Our BLI-guided analyses showed appearance of weak nLuc signals in
301 lungs of infected mice prophylactically treated with CV3-1 as well as α NK1.1 mAbs compared to
302 those in the control cohort treated with CV3-1 and with an isotype control (**Figure S7A-D**). In
303 addition, two of the mice that underwent NK cell depletion in the CV3-1 pretreated group
304 experienced a temporary but significant decrease in body weight before recovering (**Figure S7E**).
305 Nevertheless, all the mice receiving CV3-1 prophylaxis survived despite NK cell depletion (**Figure**
306 **S7F**). We did observe a marginal increase in viral loads in target organs upon NK depletion in
307 mice under CV3-1 prophylaxis (**Figure S7G**). In addition, the ability of CV3-1 to suppress
308 inflammatory cytokines was significantly compromised upon NK cell-depletion (**Figure S7H, I-K**).
309 Thus, while NK cells do contribute to *in vivo* efficacy of CV3-1, their requirement was not
310 significant enough to compromise protection offered by CV3-1 prophylaxis.

311 To investigate NK cell-requirement during CV3-1 therapy, we depleted them in SARS-
312 CoV-2-nLuc infected mice where CV3-1 treatment was initiated at 3 dpi (**Figure 7A**). Our BLI-
313 centric multiparametric analyses revealed that NK cell depletion partially compromised the
314 efficacy of CV3-1 therapy with 25% of the mice succumbing to SARS-CoV-2 infection compared
315 to CV3-1-treated controls where all the mice survived (**Figure 7B-F**). We next investigated if
316 Ly6G⁺ neutrophils and Ly6Chⁱ CD11b⁺ classical monocytes accounted for additional Fc effector

317 activities by using the anti-Ly6G and anti-CCR2 depleting mAbs in mice under CV3-1 therapy
318 (**Figure 7A, B, S7L-O**) (Mack et al., 2001). Neutrophil or monocyte depletion under CV3-1 therapy
319 led to 75% and 80% of the mice failed to control SARS-CoV-2 spread and loss in body weight
320 resulting in death although neuroinvasion was overall weaker than isotype control cohorts (**Figure**
321 **7B-E, G**). Neutrophil or monocyte depletion in the setting of CV3-1 therapy led to increased viral
322 burden and enhanced expression of *CCL2*, *CXCL10*, and *IL6* mRNA in target tissues compared
323 to the cohort under CV3-1 therapy (**Figure 7H-J**). These data indicated that neutrophils,
324 monocytes and NK cells contributed to the antibody-dependent cure of mice from lethal SARS-
325 CoV-2 infection and are critical for the success of SARS-CoV-2 NAb-directed therapies.

326 Together, our data demonstrate the utility of a BLI-guided platform for temporo-spatial
327 visualization of SARS-CoV-2 replication, pathogenesis and the mechanisms contributing to an
328 effective outcome with NAb-based interventions *in vivo* in the K18-ACE2 mouse model.

329

330 **Discussion**

331 NAb therapies are being explored to augment current vaccination strategies against
332 SARS-CoV-2 to expand the protection afforded towards newly arising virus variants. However,
333 prior evidence of antibody-dependent enhancement of pathology caused by respiratory viruses
334 like RSV and SARS-CoV-1 warrants careful investigation of antibody effects *in vivo* before clinical
335 implementation (Iwasaki and Yang, 2020; Klasse and Moore, 2020). We have established a
336 whole-body imaging approach to follow the dynamics and pathogenesis of SARS-CoV-2 infection
337 in mice to facilitate preclinical studies for identifying effective therapeutic measures against
338 COVID-19. Temporal tracking of K18-hACE2 mice revealed that SARS-CoV-2 first replicates in
339 the nasal cavity, reaches the lungs at 1 dpi where the infection expands till 3 dpi before spreading
340 systemically to other organs including the brain by 4 dpi. BLI also helped illuminate how the highly
341 potent human NAb CV3-1 (targets Spike RBD) and CV3-25 (binds S2 domain) differed in their

ability to protect or treat SARS-CoV-2 infection in the highly susceptible K18-hACE2 mouse model. Imaging analyses revealed widespread NAb distribution within the animals, including in the nasal cavity and lung where the virus initially establishes infection, and persistence for at least a week after administration, features that were critical for efficacy in this acute model for SARS-CoV-2. BLI also revealed a therapeutic window of 3 dpi for CV3-1 NAb to successfully halt progression of established infection in the lungs and distal tissues. Given that the previously reported SARS-CoV-2 NAbs have a therapeutic window of 1 dpi (Alsoussi et al., 2020; Hassan et al., 2020; Schafer et al., 2021; Winkler et al., 2021). CV3-1 displays one of the most potent *in vivo* efficacy profile with a widened therapeutic window till 3 dpi. Most protective human NAbs for SARS-CoV-2 tested in animal models and also in humans, target RBD (Baum et al., 2020; Chen et al., 2021; Rogers et al., 2020; Schafer et al., 2021; Tortorici et al., 2020; Weinreich et al., 2021), some NTD targeting NAbs also display potent antiviral activity *in vivo* (Li et al., 2021; Noy-Porat et al., 2021; Voss et al., 2020). We show that the S2-directed CV3-25 NAb also conferred protection, albeit not as potent as CV3-1. This of significance as newly emerging variants display fewer mutations in the S2 subunit compared to the S1 subunit. Indeed, CV3-25 has been found to efficiently neutralize the B.1.351 variant, while neutralization capacities of anti-NTD and anti-RBD NAbs were greatly diminished (Stamatatos et al., 2021).

Our data also establishes that neutralizing capacity alone is not enough to garner clinical protection by NAbs. LALA variants of CV3-1 revealed a crucial role for Fc-mediated interactions in augmenting *in vivo* protection for prophylaxis as well as therapy. The requirement for Fc effector functions during CV3-1 prophylaxis, needed for eliminate infected cells originating from virions that eluded neutralization, is noteworthy and contrasting to a recent report where they were required only during NAb therapy (Winkler et al., 2021). Introducing LALA mutation in CV3-1 completely compromised its ability to therapeutically cure and was in agreement with previous observations (Winkler et al., 2021). Surprisingly, we noticed a more severe loss in body weight in mice that were therapeutically administered CV3-1 LALA variants and significantly higher

368 inflammatory responses (CCL2, CXCL10, IFN γ) in lungs than isotype-treated control animals.

369 These data suggest that the Fc region plays an additional protective role by limiting

370 immunopathology through dampening of inflammatory responses. A previously reported NAb

371 engaged only monocytes for *in vivo* activity (Winkler et al., 2021). However, our studies revealed

372 that CV3-1 engaged Fc-interacting neutrophils, monocytes and NK cells for its *in vivo* efficacy.

373 Thus, in addition to its potent neutralizing activity, a superior engagement of innate immune

374 components contributed to the high *in vivo* potency of CV3-1

375 Experiments using low doses of NAbs indicated that CV3-1 did not enhance infection at

376 concentrations that protected only 50% of animals in the group. Thus, our data add to the growing

377 body of evidence that suggest the absence of an antibody-dependent enhancement (ADE)

378 mechanism with a protective rather than a pathogenic role for Fc effects during SARS-CoV-2

379 infection (Schafer et al., 2021; Winkler et al., 2021). However, while mouse Fc γ Rs bind human

380 antibodies with similar affinities as mouse antibodies, their expression pattern on various mouse

381 immune cells differs from those in humans. Therefore, additional investigations in other models

382 are required to confirm definitive absence of ADE during human SARS-CoV-2 infection (Gorman

383 et al., 2021). Moreover, elucidation of the major Fc γ R(s) (Fc γ RI, Fc γ RIII and/or Fc γ RIV) engaged

384 by NAbs will help design ultrapotent SARS-CoV-2 Nab therapies (Smith et al., 2012).

385 In summary, our study demonstrates the utility of the BLI-guided approach to study SARS-

386 CoV-2 pathogenesis and identify effective antiviral therapies for rapid translation to clinical use in

387 humans.

388

389 **Supplemental information**

390 7 Supplementary figures and 4 Videos

391 **Author contributions**

392 PDU, IU, JP, PK, AF, & WM: conceptualization, experimental design, interpretation, and
393 manuscript preparation and writing; IU: animal experiments, BLI, antibody biodistribution, viral
394 load analyses & data processing; PDU: histological analyses, FACS, data processing, figure
395 generation & initial draft; LS & ATM: isolated NAbs; JP, ML, SPA, GBB, MB, SD, RG, CF, YC,
396 AT, GG, CB, HM, GAD, JDD, DEK, JR, MP, WM and AF: generation & *in vitro* characterization of
397 SARS-CoV-2 S NAbs; MSL & PJB: EM tomography; IU, HS: cytokine, N gene mRNA PCR; MM:
398 anti-CCR2 antibody; CBW: aliquot of the reporter virus. PK, WM, AF, PJB: funding for the work.

399

400 **Acknowledgements**

401 This work was supported by NIH grants P50AI150464 to WM and PJB; R33AI122384 and
402 RO1AI145164 to PK; George Mason University Fast Grants to MSL and PJB; P20GM125498
403 (awarded to UVM Translational Global Infectious Disease Research Center) to EAB;
404 le Ministère de l'Économie et de l'Innovation du Québec, Programme
405 de soutien aux organismes de recherche et d'innovation, Foundation du CHUM, Canadian
406 Institutes of Health Research (CIHR) foundation grant #352417 & Rapid Research Funding
407 Opportunity #FRN440388 to J.D.D. and G.A.D, Canada Research Chair on Retroviral Entry no.
408 RCHS0235 950-232424 to AF; Canada's COVID-19 Immunity Task Force (CITF) & Canada
409 Foundation for Innovation (CFI) #41027 to AF and DEK & #36287 to JDD. and GAD; FRQS Merit
410 Research Scholarship to DEK; CIHR fellowships to JP, SPA and GBB,
411 MITACS Accélération postdoctoral fellowship to RG; Fred Hutch COVID-19 Research Fund to LS
412 and ATM.

413

414 **Disclaimer**

415 The views expressed in this presentation are those of the authors and do not reflect the official
416 policy or position of the Uniformed Services University, US Army, the Department of Defense, or
417 the US Government.

418

419 **Declaration of Interests**

420 The authors declare no competing interests.

421 **Figure Legends**

422 **Figure 1. Visualization of SARS-CoV-2 Replication Dynamics in hACE2 Transgenic Mice**

423 (A) Experimental strategy utilizing SARS-CoV-2 carrying nLuc reporter in ORF7 for non-invasive
424 BLI of virus spread following intranasal (i.n.) challenge of B6 or K18-hACE2 mice.

425 (B) Representative images from temporal BLI of SARS-CoV-2-nLuc-infected mice in ventral (v)
426 and dorsal (d) positions at the indicated dpi and after necropsy at 6 dpi.

427 (C) Temporal quantification of nLuc signal as flux (photons/sec) acquired non-invasively in the
428 indicated tissues of each animal. The color bar above the x-axis (yellow to orange) represents
429 computed signal intensities in K18-hACE2 mice that are significantly above those in B6 mice.

430 (D) Temporal changes in mouse body weight at the indicated dpi with initial body weight set to
431 100%.

432 (E) Kaplan-Meier survival curves of mice for experiment as in A statistically compared by log-rank
433 (Mantel-Cox) test.

434 (F) *Ex vivo* imaging of indicated organs and quantification of nLuc signal as flux(photons/sec) at
435 indicated dpi after necropsy

436 (G, H) Viral loads (FFUs/g or nLuc activity/g) from indicated tissue using Vero E6 cells as targets.
437 Undetectable virus amounts were set to 1.

438 (I) Ratio of C_t values for SARS-CoV-2 nucleocapsid (N) and nLuc estimated by RT-PCR using
439 RNA extracted from input virions (inoculum) and virions from sera of mice at 6 dpi.

440 (J, K) Cytokine mRNA levels in lung and brain tissues at 6 dpi after normalization to *Gapdh* in the
441 same sample and that in uninfected mice.

442 Each curve in (C) and (D) and each data point in (F), (I), (J), and (K) represents an individual
443 mouse. Scale bars in (B and (F) denote radiance (photons/sec/cm²/steradian). p values obtained
444 by non-parametric Mann-Whitney test for pairwise comparison. *, p < 0.05; **, p < 0.01; ***, p <
445 0.001; ****, p < 0.0001; ns, not significant; Mean values ± SD are depicted.

446

447 **Figure 2. EM localization of SARS-CoV-2 Virions in Lung, Brain and Testis of Infected K18-**
448 **hACE2 Mice.** (A) 2D overview of a lung region featuring red blood cells (rbc) within a pulmonary
449 capillary, an alveolar Type 2 cell (AT2).
450 (B) Slice from a 3D tomogram of square region in A showing membrane-enclosed cytoplasmic
451 compartments (arrowheads) containing presumptive SARS-CoV-2 virions in capillary endothelial
452 cells.
453 (C) Presumptive virions from tomogram in B displayed at equatorial views. Presumptive virions
454 were identified as described in the Methods and are directly comparable to those in SARS-CoV-
455 2 infected Vero-E6 cells (panels O-Q).
456 (D) ImmunoEM tomography of presumptive SARS-CoV-2 virions from infected lung tissue,
457 labeled with antiserum against Spike protein and gold (10 nm) conjugated 2° antibodies. Gold
458 particles localized to the outer peripheries of the virions indicate specific labeling of SARS-CoV-
459 2 Spikes.
460 (E) Tomographic of SARS-CoV-2 infected brain tissue. Presumptive SARS-CoV-2 virions (red
461 arrowheads) are present within a neuron (pale green). A dendritic synaptic terminal to the left of
462 the virus-containing neuron shows that presumptive SARS-CoV-2 virions are easily distinguished
463 from typical synaptic neurotransmitter vesicles.
464 (F) 2D overview of brain tissue illustrating the complex spatial relationship among neurons and
465 other brain cell types. Presumptive SARS-CoV-2 virions are present in two compartments (black
466 squares) within a single neuron.
467 (G, H) Tomographic slices of black squares in F. Presumptive SARS-CoV-2 virions (red
468 arrowheads) appear to be aligned within compartments that border the edges of a neural
469 projection.
470 (I) Presumptive SARS-CoV-2 virions from tomograms in G and H.
471 (J) ImmunoEM tomography as in D of presumptive SARS-CoV-2 virions from infected brain tissue.

472 (K) (Upper) BLI of testis from a SARS-CoV-2 infected mouse to identify infected regions for IF
473 and EM analyses. (Lower) IF image of an infected testis region stained with antibodies to SARS-
474 CoV-2 Nucleocapsid (red)

475 (L) 2D overview of testis corresponding to region of high intensity (red) in the upper panel of K,
476 showing Sertoli cells surrounded by developing sperm (left) and one primary spermatocyte (1°S,
477 upper right). Presumptive SARS-CoV-2 virions are localized to membrane-bound compartments
478 in Sertoli cells (black squares).

479 (M, N) Slices from two 3D tomograms of squares in L. Presumptive SARS-CoV-2 virions
480 (arrowheads) are present within membrane-enclosed cytoplasmic compartments. These
481 compartments contain additional structures amongst the discernable SARS-CoV-2 virions
482 (insets).

483 (O) EM localization of virions in SARS-CoV-2 infected Vero-E6 cells, processed for EM as above
484 tissue samples. Virions were characterized (see Methods) and compared to presumptive virions
485 in the tissue samples to confidently verify their identities. 2D overview of infected Vero-E6 cell in
486 a 150 nm section.

487 (P) Tomogram of rectangle in O showing >100 presumptive SARS-CoV-2 virions contained within
488 cytoplasmic exit compartments.

489 (Q) Virions from the tomogram in P showing common features of dense RNC puncta, discernable
490 surface spikes, vary in size (~60-120 nm) and shape. Virions are directly comparable to those
491 shown for the tissue samples in C and I.

492

493 **Figure 3. *In vitro* Characterization of CV3-1 and CV3-25 NAbs.** (A) NAb binding to SARS-CoV-
494 2 Spike ectodomain (S-6P) or RBD estimated by ELISA. Relative light unit (RLU) were normalized
495 to the cross-reactive SARS-CoV-1 NAb CR3022. NAb binding to SARS-CoV-2 S2 N-His protein
496 on cell-surface of transfected 293T cells analyzed by flow cytometry. Median fluorescence

497 intensities (MFIs) for anti-Spike NAbs were normalized to the signal obtained with an anti-His tag
498 mAb.

499 (B) Flow cytometric detection of S-expressing 293T cells from the different human CoVs: SARS-
500 CoV-2, SARS-CoV-1, OC43, HKU1, MERS-CoV, NL63 and 229E. MFI from 293T cells
501 transfected with empty vector were used for normalization.

502 (C) Pseudoviruses bearing SARS-CoV-2 or SARS-CoV-1 S were tested for capture by anti-
503 Spike NAbs. The cross-reactive CR3022 mAb was used for normalization.

504 (D-E) NAb binding affinity and kinetics to SARS-CoV-2 S using Surface Plasmon Resonance
505 (SPR). SARS-CoV-2 S-6P or S2 ectodomain was immobilized as the ligand on the chip and CV3-
506 1 or CV3-25 Fab was used as analytes at concentrations in a range from 1.56 to 100 nM for both
507 Fabs to S-6P and 3.125nM to 200nM for CV3-25 to S2 (2-fold serial dilution, see Methods for
508 details). Alternatively, CV3-1 IgG was immobilized on the chip and SARS-CoV-2 RBD was used
509 as the analyte with concentrations ranging from 1.56 to 50 nM (2-fold serial dilution). Kinetic
510 constants were determined using a 1:1 Langmuir model in BIA evaluation software (experimental
511 readings shown in blue and fitted curves shown in black).

512 (F-H) FRET histograms of ligand-free S on S-MEN coronavirus-like particles (VLPs) or in
513 presence of 50 µg/mL of CV3-1 (G) or CV3-25 (H). VLPs were incubated for 1 h at 37°C before
514 smFRET imaging. N_m is the number of individual FRET traces compiled into a conformation-
515 population FRET histogram (gray lines) and fitted into a 4-state Gaussian distribution (solid black)
516 centered at 0.1-FRET (dashed cyan), 0.3-FRET (dashed red), 0.5-FRET (dashed green), and 0.8-
517 FRET (dashed magenta).

518 (I) Neutralizing activity of CV3-1 and CV3-25 alone or in combination (1:1 ratio) on SARS-CoV-2
519 S bearing pseudoviruses using 293T-ACE2 cells.

520 (J) Microneutralization activity of anti-Spike NAbs on live SARS-CoV-2 virus using Vero E6 cells.

521 (K) Inhibition of cell-to-cell fusion between 293T cells expressing HIV-1 Tat and SARS-CoV-2 S
522 and TZM-bl-ACE2 cells by NAbs.

523 Half maximal inhibitory antibody concentration (IC_{50}) values in I-K were determined by normalized
524 non-linear regression analyses.

525 (L) MFI of CEM.NKr cells expressing SARS-CoV-2 Spike (CEM.NKr-Spike) stained with indicated
526 amounts of NAbs and normalized to parental CEM.NKr.

527 (M) % ADCC in the presence of titrated amounts of NAbs using 1:1 ratio of parental CEM.NKr
528 cells and CEM.NKr-Spike cells as targets when PBMCs from uninfected donors were used as
529 effector cells

530 (N) % ADCP in the presence of titrated amounts of NAbs using CEM.NKr-Spike cells as targets
531 and THP-1 cells as phagocytic cells.

532

533 **Figure 4. Prophylactic Treatment with CV3-1 Protects Mice from Lethal SARS-CoV-2**

534 **Infection.** (A) Experimental design for testing *in vivo* efficacy of NAbs CV3-1 and CV3-25
535 administered alone (12.5 mg/kg body weight) or as a 1:1 cocktail (6.25 mg/kg body weight each)
536 1 day prior to challenging K18-hACE2 mice (i.n.) with SARS-CoV-2-nLuc followed by non-invasive
537 BLI every 2 days. Human IgG1-treated (12.5 mg Ig/kg) mice were use as the isotype control (Iso)

538 (B) Representative images from BLI of SARS-CoV-2-nLuc-infected mice in ventral (v) and dorsal
539 (d) positions at the indicated dpi and after necropsy at indicated days for experiment as in A.

540 (C-D) Temporal quantification of nLuc signal as flux (photons/sec) computed non-invasively in
541 indicated areas of each animal.

542 (E) Temporal changes in mouse body weight at the indicated dpi with initial body weight set to
543 100%.

544 (F) Kaplan-Meier survival curves of mice statistically compared by log-rank (Mantel-Cox) test for
545 experiment as in A.

546 (G, H) *Ex-vivo* imaging of organs and quantification of nLuc signal as flux (photons/sec) at the
547 indicated dpi after necropsy.

548 (I) Viral loads (nLuc activity/g) from indicated organs using Vero E6 cells as targets. Undetectable
549 virus amounts were set to 1.
550 (J, K) Cytokine mRNA levels in lung and brain tissues after necropsy normalized to *Gapdh* in the
551 same sample and that in uninfected mice.
552 Viral loads (I) and inflammatory cytokine profile (J, K) were determined after necropsy for mice
553 that succumbed to infection and in mice surviving at 22 dpi.
554 Scale bars in (B) and (G) denote radiance (photons/sec/cm²/steradian). Each curve in (C)-(E) and
555 each data point in (H)-(K) represents an individual mouse. Grouped data in (C)-(K) were analyzed
556 by 2-way ANOVA followed by Dunnett's or Tukey's multiple comparison tests. Statistical
557 significance for group comparisons to isotype control are shown in black and for those to CV3-25
558 are shown in red *, p < 0.05; **, p < 0.01; ***, p < 0.001; ****, p < 0.0001; Mean values ± SD are
559 depicted.
560

561 **Figure 5. CV3-1 Therapy Protects Mice from Lethal SARS-CoV-2 Infection.** (A) Experimental
562 design to test *in vivo* efficacy of CV3-1 administered i.p. (12.5 mg/kg body weight) at indicated
563 times after i.n. challenge of K18-hACE2 mice with SARS-CoV-2 nLuc followed by non-invasive
564 BLI every 2 days. Human IgG1 treated (12.5 mg/kg body weight) mice were the control cohort.
565 (B) Representative images from temporal BLI of SARS-CoV-2-nLuc-infected mice in ventral (v)
566 and dorsal (d) positions at the indicated dpi and after necropsy.
567 (C-D) Temporal quantification of nLuc signal acquired non-invasively as flux (photons/sec) in
568 indicated regions of each mice.
569 (E) Temporal changes in mouse body weight at indicated dpi with initial body weight set to 100%.
570 (F) Kaplan-Meier survival curves of mice statistically compared by log-rank (Mantel-Cox) test for
571 experiment as in A.

572 (G, H) *Ex vivo* imaging of indicated organs and quantification of nLuc signal as flux(photon/sec)
573 at indicated dpi after necropsy.
574 (I) Viral loads estimated as nLuc activity/g of indicated organs using Vero E6 cells as targets.
575 Non-detectable virus amounts were set to 1.
576 (J, K) Cytokine mRNA levels in lung and brain tissues after necropsy. The data was normalized
577 to *Gapdh* in the same sample and that in uninfected mice.
578 Viral loads (I) and inflammatory cytokine profile (J, K) were determined after necropsy at times
579 indicated in G. Each curve in (C)-(E) and each data point in (H)-(K) represents an individual
580 mouse. CV3-1 treatment times are indicated in (C)-(E). Grouped data in (C)-(K) were analyzed
581 by 2-way ANOVA followed by Dunnett's or Tukey's multiple comparison tests. Statistical
582 significance for group comparisons to isotype control are shown in black and for those under CV3-
583 1 therapies to 4 dpi-treated cohorts are shown in red. *, p < 0.05; **, p < 0.01; ***, p < 0.001;
584 ****, p < 0.0001; Mean values ± SD are depicted.
585

586 **Figure 6. Fc-mediated Antibody Effector Functions Contribute to the *In Vivo* Efficacy of**
587 **CV3-1** (A) Experimental design to test therapeutic efficacy of NAb CV3-1 and its corresponding
588 Leucine to Alanine (LALA) mutant administered ip (12.5 mg/kg body weight) 3 dpi to K18-hACE2
589 mice challenged with SARS-CoV-2 nLuc followed by non-invasive BLI every 2 days. Human IgG1-
590 treated (12.5 mg/kg body weight) mice were used as the control cohort.
591 (B) Representative images from temporal BLI of SARS-CoV-2-nLuc-infected mice in ventral (v)
592 and dorsal (d) positions at the indicated dpi and after necropsy. Scale bars denote radiance
593 (photons/sec/cm²/steradian).
594 (C-D) Temporal quantification of nLuc signal acquired non-invasively as flux (photons/sec) in
595 indicated regions.
596 (E) Temporal changes in mouse body weight at indicated dpi with initial body weight set to 100%.

597 (F) Kaplan-Meier survival curves of mice statistically compared by log-rank (Mantel-Cox) test. for
598 experiment as in A.

599 (G) Viral loads (nLuc activity/g) in indicated organs using Vero E6 cells as targets. Undetectable
600 virus amounts were set to 1.

601 (H, I) Cytokine mRNA levels in lung and brain tissues after necropsy. The values were normalized
602 to *Gapdh* in the same sample and that in uninfected mice.

603 Viral loads (G) and inflammatory cytokine profile (H, I) was determined after necropsy at times
604 indicated in B. Each curve in (C)-(E) and each data point in (G)-(I) represents an individual mouse.
605 CV3-1 treatment times are indicated in (C)-(E). Grouped data in (C)-(I) were analyzed by 2-way
606 ANOVA followed by Dunnett's or Tukey's multiple comparison tests. Statistical significance for
607 group comparisons to isotype control are shown in black and between CV3-1 and CV3-1 LALA
608 treated cohorts are shown in red. *, p < 0.05; **, p < 0.01; ***, p < 0.001; ****, p < 0.0001; Mean
609 values ± SD are depicted.

610

611 **Figure 7. Monocytes, Neutrophils and Natural Killer Cells Contribute to Antibody Effector**
612 **Functions In Vivo.** (A) Experimental design to test the contribution of NK cells, neutrophils
613 (CD11b⁺Ly6G⁺) and monocytes (CCR2⁺Ly6^{hi} CD11b⁺) in K18-hACE2 mice therapeutically treated
614 with CV3-1 NAb (i.p., 12.5 mg/kg body weight) at 3 dpi after challenge with SARS-CoV-2-nLuc.
615 αNK1.1 mAb (i.p., 20 mg/kg body weight), αLy6G mAb (i.p., 20 mg/kg body weight) and αCCR2
616 mAb (i.p., 2.5 mg/kg body weight) were used to deplete NK cells, neutrophils and monocytes
617 respectively every 48h starting at 1 dpi. Corresponding human (for CV3-1) and rat (for αNK1.1
618 and αLy6G mAb or αCCR2) monoclonal antibodies served as non-specific isotype controls (Iso).
619 The mice were followed by non-invasive BLI every 2 days from the start of infection.
620 (B) Representative images from temporal BLI of SARS-CoV-2-nLuc-infected mice in ventral (v)
621 and dorsal (d) positions at the indicated dpi and after necropsy.

622 (C-D) Temporal quantification of nLuc signal acquired non-invasively as flux (photons/sec) in
623 indicated regions.

624 (E) Temporal changes in mouse body weight at indicated dpi with initial body weight set to 100%.

625 (F) Kaplan-Meier survival curves of mice statistically compared by log-rank (Mantel-Cox) test for
626 experiment as in A.

627 (H) Viral loads (nLuc activity/g) of indicated organs using Vero E6 cells as targets. Undetectable
628 virus amounts were set to 1.

629 (I, J) Cytokine mRNA levels in lung and brain tissues after necropsy and normalization to GAPDH
630 in the same sample and that in uninfected mice.

631 Viral loads (H) and inflammatory cytokine profile (I, J) was determined after necropsy at times
632 indicated in B. Each curve in C-E and each data point in H-J represents an individual mouse.

633 Grouped data in (C)-(I) were analyzed by 2-way ANOVA followed by Dunnett's or Tukey's multiple
634 comparison tests. Statistical significance: group comparisons to isotype control are shown in
635 black; group comparisons to Iso+CV3-1 within the NK and neutrophil depleted cohorts are shown
636 in purple; group comparisons to Iso+CV3-1 within the monocyte-depleted cohorts are shown in
637 red. *, p < 0.05; **, p < 0.01; ***, p < 0.001; ****, p < 0.0001; Mean values ± SD are depicted.

638 **Supplementary Figure Legends:**

639 **Figure S1. Widespread SAR-CoV-2 infection in K18-hACE2 mice. Related to Figure 1.** (A) A
640 plot showing real-time PCR analyses to detect SARS-CoV-2 nucleocapsid (N) gene mRNA in
641 indicated organs of B6 and K18-hACE2 mice at 6 dpi intranasally challenged with 1×10^5 FFU of
642 SARS-CoV-2-nLuc. The data were normalized to N RNA seen in uninfected mice and GAPDH
643 mRNA levels. *p* values obtained by non-parametric Mann-Whitney test for pairwise comparison.

644 *, *p* < 0.05; **, *p* < 0.01; ***, *p* < 0.001; ****, *p* < 0.0001; ns, not significant; Mean values \pm SD
645 are depicted.

646 (B) Images of cryosections from indicated tissues of SARS-CoV-2-nLuc infected K18-hACE2
647 mouse harvested at 6 dpi. Actin (green), nucleocapsid (red) and hACE2 (magenta) were detected
648 using phalloidin and respective antibodies. Notably, hACE2 appeared as puncta on the surface
649 of infected neurons and lung tissue compared to other organs where the signal was more uniform
650 and stained a region of the cell surface. Scale bar: 50 μ m

651 (C) Images of cryosections from brain tissues of SARS-CoV-2-nLuc infected K18-hACE2 mouse
652 harvested at 6 dpi to characterize infected cells. Glial cells (top panel) were identified using
653 antibodies to markers CD68 (magenta) and CD11b (green). Neurons (lower panel) were identified
654 using antibodies to MAP2 (green) and mature astrocytes were identified using antibodies to GFAP
655 (magenta). SARS-CoV-2 infected cells were identified using antibodies to nucleocapsid (red).
656 Nucleocapsid positive cells were predominantly positive for MAP2. Scale bar: 20 μ m

657

658 **Figure S2. Widespread biodistribution of CV3-25 and CV3-1 NAbs in mice 24 h after
659 intraperitoneal delivery. Related to Figure 3.** (A) C57BL/6J mice were either mock treated
660 (PBS) or intraperitoneally administered 12.5 mg/kg body weight of CV3-25 monoclonal antibody
661 conjugated to Alexa Fluor 594 (CV3-25 AF594). 24 h later, indicated tissues were imaged using
662 the fluorescence module in IVIS spectrum to detect AF594. The plot shows the quantified

663 radiance detected in indicated tissues after normalization with corresponding organs from control
664 mouse.

665 (B) Images of cryosections from indicated tissues from CV3-25 AF594-treated mouse as in A.
666 Actin and CV3-25 were detected using phalloidin-AF488 and AF647 conjugated anti-human IgG
667 respectively. Scale bar: 20 μ m

668 (C) C57BL/6J mice were either mock treated (PBS) or intraperitoneally administered 12.5
669 mg/kg of CV3-1 monoclonal antibody conjugated to Alexa Fluor 647 (CV3-25 AF647). 24 h later,
670 indicated tissues were imaged using the fluorescence module in IVIS spectrum to detect AF647.
671 The plot shows the quantified radiance detected in indicated tissues after normalization with
672 corresponding organs from control mouse.

673 (B) Images of cryosections from indicated tissues from CV3-1 AF647-treated mouse as in A. Actin
674 was detected using phalloidin-Alexa Fluor 488. CV3-1 AF647 was detected in the red channel
675 using Alexa Fluor 568 conjugated anti-human IgG. Scale bar: 20 μ m

676

677 **Figure S3. Assessment of CV3-1 and CV3-25 NAbs biodistribution in mice using ELISA and**
678 **immunohistology. Related to Figure 4.** (A-D) Estimation of CV3-25 and CV3-1 NAbs
679 biodistribution in mice using ELISA. Measurement of anti-Spike NAbs levels in organs was
680 performed using quantitative ELISA. (A-B) Recombinant SARS-CoV-2 RBD and (C-D) S-6P
681 proteins were used to quantify CV3-1 and CV3-25 antibody levels, respectively. Linear standard
682 curves using known concentrations of CV3-1 or CV3-25 NAbs were established for inferring the
683 antibody concentration in organ homogenates. Serial dilutions of homogenized mice organs were
684 prepared in PBS and incubate on antigen-coated plates. The presence of anti-Spike NAbs was
685 revealed using HRP-conjugated anti-human IgG secondary Abs. The signal obtained with BSA
686 (negative control) was subtracted for each organ. Relative light unit (RLU) values were
687 transformed into a NAb concentrations based on the standard curve and the dilution

688 factor. Subsequently, these concentration values were multiplied with the homogenization volume
689 and divided by the total organ weight.

690 (E) Persistence and redistribution of neutralizing NAbs in SARS-CoV-2 infected mice. Images of
691 brain tissue from K18-hACE2 mice infected with SARS-CoV-2-nLuc at 6 dpi that were
692 prophylactically treated with CV3-1 or CV3-25 (12.5 mg/kg body weight), 24 h before infection.
693 Actin (green) was labelled using phalloidin, CV3-1 and CV3-25 (magenta) were detected using
694 anti-hIgG conjugated to Alexa Fluor 647 and infected cells (red) were identified using antibodies
695 to SARS-CoV-2 N. CV3-1 localizes to the endothelial walls of blood vessels and CV3-25
696 redistributes to decorate infected neurons in addition to endothelium (seen in UI mice; Figure S2).

697 Scale bar: 50 µm

698

699 **Figure S4. Efficacious dose for CV3-1 NAb during prophylaxis. Related to Figure 4.** (A) A
700 scheme showing experimental design for testing the dose of CV3-1 NAb to achieve protection for
701 lethal SARS-CoV-2-nLuc infection. Indicated concentration of CV3-1 NAb was delivered (i.p.) 1
702 day before challenging K18-hACE2 mice with 1×10^5 FFU of SARS-CoV-2 nLuc. Human IgG1-
703 treated (12.5 mg/kg) mice were used as control (isotype treated). Mice were followed by non-
704 invasive BLI every 2 days from the start of infection using IVIS Spectrum after retroorbital
705 administration of furimazine (nLuc substrate).

706 (B) SARS-CoV-2 replication and dissemination in K18-hACE2 transgenic mice ($n = 4-6$ per group)
707 for experiment as in A, were monitored via BLI in ventral (v) and dorsal (d) positions at the
708 indicated days post infection every 2 days. Images from two mice under CV3-1 prophylaxis (0.7
709 mg/kg) are shown where one mouse succumbed at 6 dpi and the other survived despite weak but
710 observable neuroinvasion. Images from one representative experiment are shown for the rest.
711 (C-D) A plot showing temporal quantification of nLuc signal acquired non-invasively and displayed
712 as photon flux (photons/sec) in whole body or brain region of SARS-CoV2-nLuc infected K18-

713 hACE2 mice for an experiment as in A. Each curve represents luminescent signal computed for
714 individual mouse. Scale bars denote radiance in photons per second per square centimeter per
715 steradian (p/sec/cm²/sr).

716 (E) A plot showing temporal body weight changes in indicated groups of K18-hACE2 mice at
717 indicated days post infection for an experiment shown in A. Each curve represents one animal.
718 The body weight at the start of the experiment was set to 100 %.

719 (F) Kaplan-Meier survival curves of mice statistically compared by log-rank (Mantel-Cox) test for
720 experiment as in A.

721 (G) Plot showing viral loads as nLuc activity per gram of indicated organs using Vero E6 cells as
722 targets. Undetectable virus amounts were set to 1 for display on log plots.
723 Grouped data in (C)-(E) and G were analyzed by 2-way ANOVA followed by Dunnett's or Tukey's
724 multiple comparison tests. Statistical significance: group comparisons to isotype control are
725 shown in black; group comparisons to CV3-1 (0.7 mg/kg) are shown in red. *, p < 0.05; **, p <
726 0.01; ***, p < 0.001; ****, p < 0.0001; Mean values ± SD are depicted.

727

728 **Figure S5. LALA mutations Diminish Antibody Effector Functions of CV3-1 and CV3-25**
729 **without Compromising Neutralizing Activity. Related to Figure 6.** (A) Cell-surface staining
730 of CEM.NKr cells stably expressing full-length SARS-CoV-2 Spike (CEM.NKr-Spike) using CV3-
731 1 and CV3-25 mAbs or their LALA mutant counterpart. The graph shown represent the mean
732 fluorescence intensities (MFI) obtained with titrated concentrations of anti-Spike NAbs. MFI
733 values obtained with parental CEM.NKr were subtracted.

734 (B) Pseudoviral particles encoding for the luciferase reporter gene and bearing the SARS-CoV-2
735 S glycoproteins were used to infect 293T-ACE2 cells. Neutralizing activity was measured by
736 incubating pseudoviruses with titrated concentrations of anti-Spike NAbs at 37°C for 1 h prior to
737 infection of 293T-ACE2 cells. Neutralization half maximal inhibitory antibody concentration (IC₅₀)

738 values were determined using a normalized non-linear regression using GraphPad Prism
739 software.

740 (C) Using a FACS-based ADCC assay, CEM.NKr parental cells were mixed at a 1:1 ratio
741 with CEM.NKr-Spike cells and were used as target cells. PBMCs from uninfected donors were
742 used as effector cells. The graph shown represent the percentages of ADCC obtained in the
743 presence of titrated concentrations of anti-Spike NAbs.

744 (D) Using a FACS-based ADCP assay, CEM.NKr-Spike cells were used as target cells and THP-
745 1 monocytic cell line was used as effector cells. The graph shown represent the percentages
746 of effector cells that had phagocytosed target cells obtained in the presence of titrated
747 concentrations of anti-Spike NAbs.

748 Statistical significance was tested using a non-parametric Mann-Whitney test for pairwise
749 comparison between WT and LALA NAb (*, p < 0.05; **, p < 0.01; ns, not significant)

750 (E-F) Biodistribution of CV3-25 and CV3-1 LALA mutants in mice 24 h after i.p. delivery. B6 mice
751 were either isotype treated (control) or intraperitoneally administered of Alexa Fluor 647
752 conjugated LALA mutants of CV3-25 or CV3-1 NAb mutants (12.5 mg/kg body weight). 24 h later,
753 indicated tissues were imaged using the fluorescence module in IVIS spectrum to detect Alexa
754 Flour 647. The plot shows the quantified radiance detected in indicated tissues after normalization
755 with corresponding organs from control mouse.

756 (G, H) Images of cryosections from brain tissues of K18-hACE2 mice pretreated with LALA
757 mutants of CV3-25 or CV3-1 (i.p., 12.5 µg/g body weight) at 6 dpi. Actin was detected using
758 phalloidin-Alexa Fluor 488. CV3-25 and CV3-1 (magenta) were detected using Alexa Fluor 647
759 conjugated anti-human IgG respectively. Infected cells were detected using antibodies to SARS-
760 CoV-2 nucleocapsid (red). Images show penetration of both CV3-25 and CV3-1 mAbs into the
761 brain and localization to the surface of infected neurons. Scale bar: 20 µm

762 (I) SARS-CoV-2 can establish infection in nasal cavity and lungs during CV3-1 prophylaxis. A
763 scheme showing experimental design to test establishment of virus infection in K18-hACE2 mice
764 pretreated with CV3-1 NAb (i.p., 12.5 mg/kg body weight), 1 day before challenging with 1×10^5
765 FFU of SARS-CoV-2 nLuc. Mice treated similarly with Isotype matched hIgG1 were used as
766 controls. The mice were followed by non-invasive BLI at 0 and 3 dpi using IVIS Spectrum after
767 retroorbital administration of furimazine (nLuc substrate).

768 (J) SARS-CoV-2 replication and dissemination in indicated groups of K18-hACE2 transgenic mice
769 ($n = 5-3$ per group) for experiment as in I, were monitored via BLI at the indicated times. The mice
770 were euthanized at 3 dpi and imaged again after necropsy. Images from one representative
771 experiment are shown.

772 (K) A plot showing temporal quantification of nLuc signal acquired non-invasively and displayed
773 as photon flux (photons/sec) in whole body of SARS-CoV2-nLuc infected K18-hACE2 mice for an
774 experiment as in I. Each line represents luminescent signal computed for individual mouse.

775 (L, M) *Ex vivo* imaging of indicated organs after necropsy at 3 dpi and quantification of nLuc
776 signal displayed as photon flux (photons/sec) in K18-ACE2 mice for experiment as in I.

777 (N) A plot showing real-time PCR analyses to detect SARS-CoV-2 nucleocapsid (N) gene mRNA
778 in indicated organs of K18-hACE2 mice for an experiment as in I. The data were normalized to N
779 gene mRNA seen in uninfected mice and *Gapdh* mRNA levels. Scale bars denote radiance
780 (photons/sec/cm²/steradian). *p* values obtained by non-parametric Mann-Whitney test for pairwise
781 comparison with isotype-treated controls; *, *p* < 0.05; **, *p* < 0.01; ***, *p* < 0.001; ****, *p* < 0.0001;
782 individual data points along with mean values \pm SD are depicted.

783

784 **Figure S6. Fc-mediated Antibody Effector Functions Contribute to *In Vivo* Efficacy of CV3-
785 1 and CV3-25 During Prophylaxis. Related to Figure 6.** (A) A scheme showing experimental
786 design for testing *in vivo* efficacy of neutralizing antibody CV3-1, CV3-25 and their corresponding

787 Leucine to Alanine (LALA) mutants (12.5 mg/kg body weight) delivered intraperitoneally (i.p.) 1
788 day before challenging K18-hACE2 mice with 1×10^5 FFU of SARS-CoV-2 nLuc. Human IgG1-
789 treated (12.5 mg/kg body weight) mice were used as control (Iso). Mice were followed by non-
790 invasive BLI every 2 days from the start of infection using IVIS Spectrum after retroorbital
791 administration of furimazine (nLuc substrate).

792 (B) SARS-CoV-2 replication and dissemination in K18-hACE2 transgenic mice ($n = 4-8$ per group)
793 for experiment as in A, were monitored via BLI in ventral (v) and dorsal (d) positions at the
794 indicated days post infection every 2 days. The mice were euthanized on indicated days and
795 imaged again after necropsy. Images from one representative experiment are shown.

796 (C-D) A plot showing temporal quantification of nLuc signal acquired non-invasively and displayed
797 as Flux (photons/sec) in whole body or brain region of SARS-CoV2-nLuc infected K18-hACE2
798 mice for an experiment as in A. Each curve represents luminescent signal computed for individual
799 mouse.

800 (E) A plot showing temporal body weight changes of K18-hACE2 mice at indicated days post
801 infection for an experiment shown in A. Each curve represents one animal. The body weight at
802 the start of the experiment was set to 100%.

803 (F) Kaplan-Meier survival curves of mice statistically compared by log-rank (Mantel-Cox) test for
804 experiment as in A.

805 (G, H) *Ex vivo* imaging of indicated organs after necropsy at indicated dpi and quantification of
806 nLuc signal displayed as Flux (photons/sec) in K18-ACE2 mice for experiment as in A.

807 (I) Plot showing viral loads as nLuc activity per gram of indicated organs using Vero E6 cells as
808 targets. Nluc activity was determined 24 h after infection. Undetectable virus amounts were set to
809 1 for display on log plots.

810 (J, K) A plot showing mRNA levels of indicated cytokines from lung and brain tissues of K18-
811 hACE2 mice at the time of euthanasia as shown in F. The mRNA amounts were normalized to
812 the levels seen in uninfected mice and the house keeping gene *Gapdh*.

813 Scale bars in (B) and (G) denote radiance (photons/sec/cm²/steradian). Grouped data in (C)-(E)
814 and (H)-(K) were analyzed by 2-way ANOVA followed by Dunnett's or Tukey's multiple
815 comparison tests. Statistical significance: group comparisons to isotype control are shown in
816 black; group comparisons between CV3-25 LALA and CV3-25 treated cohorts are shown in red;
817 group comparison between CV3-1 LALA and CV3-1 treated cohorts are shown in purple. *, p <
818 0.05; **, p < 0.01; ***, p < 0.001; ****, p < 0.0001; Mean values ± SD are depicted.

819

820 **Figure S7. NK Cells Contribute Marginally to *In Vivo* Efficacy During CV3-1 Prophylaxis.**

821 **Related to Figure 7.** (A) A scheme showing experimental design for testing the contribution of
822 NK cells in K18-hACE2 mice pretreated with CV3-1 NAb (i.p., 12.5 mg/kg body weight), 1 day
823 before challenging with 1 x 10⁵ FFU of SARS-CoV-2 nLuc. αNK1.1 mAb (i.p., 20 mg/kg body
824 weight) was used to deplete NK cells at indicated time points. Corresponding human (for CV3-1)
825 and rat (for αNK1.1) antibodies served as non-specific isotype controls. The mice were followed
826 by non-invasive BLI every 2 days from the start of infection using IVIS Spectrum after retroorbital
827 administration of furimazine (nLuc substrate).

828 (B) SARS-CoV-2 replication and dissemination in indicated groups of K18-hACE2 transgenic mice
829 (n = 5 per group) for experiment as in A, were monitored via BLI at ventral (v) and dorsal (d)
830 positions at the indicated days post infection every 2 days. The mice were euthanized at indicated
831 times and imaged again after necropsy. Images from one representative experiment are shown.

832 (C-D) A plot showing temporal quantification of nLuc signal acquired non-invasively and displayed
833 as photon flux (photons/sec) in whole body or brain region of SARS-CoV2-nLuc infected K18-
834 hACE2 mice for an experiment as in A. Each curve represents luminescent signal computed for
835 individual mouse. Scale bars denote radiance (photons/sec/cm²/steradian).

836 (E) A plot showing temporal body weight changes in designated groups of K18-hACE2 mice at
837 indicated days post infection for an experiment shown in A. Each curve represents one animal.
838 The body weight at the start of the experiment was set to 100%.

839 (F) Kaplan-Meier survival curves of mice statistically compared by log-rank (Mantel-Cox) test for
840 experiment as in A.

841 (G) Plot showing viral loads as nLuc activity per gram of indicated organs using Vero E6 cells as
842 targets. Nluc activity was determined 24 h after infection. Undetectable virus amounts were set to
843 1 for display on log plots.

844 (H, I) A plot showing mRNA levels of indicated cytokines from lung and brain tissues of K18-
845 hACE2 mice at the time of euthanasia as shown in F. The mRNA amounts were normalized to
846 the levels seen in uninfected mice and the house keeping gene GAPDH.

847 (J, K) Representative FACS plots showing the gating strategy to identify NK cells (CD3-NK1.1⁺)
848 and quantification to ascertain their depletion in PBMCs of indicated groups of mice.

849 (L, M) Representative FACS plots showing the gating strategy to identify neutrophils cells (CD45⁺
850 CD11b⁺Ly6G⁺) and quantification to ascertain their depletion in PBMCs of indicated groups of
851 mice.

852 (N, O) Representative FACS plots showing the gating strategy to identify Ly6C^{hi} monocytes and
853 quantification to ascertain their depletion in PBMCs of indicated groups of mice.

854 Grouped data in (C)-(E) and (G)-(I) were analyzed by 2-way ANOVA followed by Dunnett's or
855 Tukey's multiple comparison tests. Statistical significance: group comparisons to isotype control
856 are shown in black; group comparisons to Iso+CV3-1 treated cohort are in red. Pairwise
857 comparisons in (K), (M) and (O) were analyzed using non-parametric Mann-Whitney test. *, p <
858 0.05; **, p < 0.01; ***, p < 0.001; ****, p < 0.0001; Mean values ± SD are depicted.

859

860 **Supplementary Multimedia Files:**

861 **Video S1. Longitudinal Non-invasive BLI of SARS-CoV-2-nLuc infection and dissemination**
862 **in K18-hACE2 mice, Related to Figure 1.** SARS-CoV-2-nLuc challenged mice were imaged
863 daily in dorsal (d) and ventral (v) positions for 6 days using IVIS Spectrum to monitor virus spread
864 in the whole body as well as neuroinvasion.

865

866 **Video S2. Tomographic Reconstruction of SARS-CoV-2 Infected Lung Tissue, Related to**
867 **Figure S2, panels B-D.** Virus particles are found within membrane-enclosed exit compartments
868 of two adjacent pulmonary capillary endothelial cells. The movie traverses the reconstructed
869 volume to illustrate the compartments (red arrowheads) then increases in magnification to detail
870 the virions within the compartments.

871 **Video S3. Tomographic Reconstruction of SARS-CoV-2 Infected Brain Tissue, Related to**
872 **Figure S2, panel F.** Virus particles are found within neurons, often appearing in linear groups
873 within compartments bordering the edges of neuronal projections. The movie details the
874 distinction between presumptive SARS-CoV-2 virions and typical synaptic neurotransmitter
875 vesicles found in an adjacent synaptic terminal.

876

877 **Video S4. Tomographic Reconstruction of SARS-CoV-2 Infected Testis Tissue, Related to**
878 **Figure S2, panel M.** Virus particles are found within membrane-enclosed compartments of Sertoli
879 cells. Additional material and structures coexist with the virions in these compartments,
880 suggesting they may be defined as lysosomes. Presumptive SARS-CoV-2 virions can be
881 discerned from the other structures.

882 **RESOURCE AVAILABILITY**

883 **Lead Contact**

884 Further information and requests for resources and reagents should be directed to and will be
885 fulfilled by the Lead Contact, Pradeep Uchil (pradeep.uchil@yale.edu), Priti Kumar
886 (priti.kumar@yale.edu), Andrés Finzi (andres.finzi@umontreal.ca) and Walther
887 Mothes(walther.mothes@yale.edu).

888 **Materials Availability**

889 All other unique reagents generated in this study are available from the corresponding authors
890 with a completed Materials Transfer Agreement.

891 **Data and Code Availability**

892 The data that support the findings of this study are available from the corresponding authors
893 upon reasonable request.

894

895 **EXPERIMENTAL MODEL AND SUBJECT DETAILS**

896

897 **Cell and Viruses**

898 Vero E6 (CRL-1586, American Type Culture Collection (ATCC), were cultured at 37°C in RPMI
899 supplemented with 10% fetal bovine serum (FBS), 10 mM HEPES pH 7.3, 1 mM sodium pyruvate,
900 1× non-essential amino acids, and 100 U/ml of penicillin–streptomycin. The 2019n-
901 CoV/USA_WA1/2019 isolate of SARS-CoV-2 expressing nanoluciferase was obtained from Craig
902 B Wilen, Yale University and generously provided by K. Plante and Pei-Yong Shi, World
903 Reference Center for Emerging Viruses and Arboviruses, University of Texas Medical Branch)
904 (Xie et al., 2020a; Xie et al., 2020b). The SARS-CoV-2 USA-WA1/2020 virus strain used for
905 microneutralization assay was obtained through BEI Resources. Virus was propagated in Vero-
906 E6 by infecting them in T150 cm² flasks at a MOI of 0.1. The culture supernatants were collected
907 after 72 h when cytopathic effects were clearly visible. The cell debris was removed by
908 centrifugation and filtered through 0.45-micron filter to generate virus stocks. Viruses were
909 concentrated by adding one volume of cold (4 °C) 4x PEG-it Virus Precipitation Solution (40 %
910 (w/v) PEG-8000 and 1.2 M NaCl; System Biosciences) to three volumes of virus-containing
911 supernatant. The solution was mixed by inverting the tubes several times and then incubated at
912 4 °C overnight. The precipitated virus was harvested by centrifugation at 1,500 × g for 60 minutes
913 at 4 °C. The concentrated virus was then resuspended in PBS then aliquoted for storage at –80°C.
914 All work with infectious SARS-CoV-2 was performed in Institutional Biosafety Committee
915 approved BSL3 and A-BSL3 facilities at Yale University School of Medicine or the University of
916 Western Ontario using appropriate positive pressure air respirators and protective equipment.

917 CEM.NKr, CEM.NKr-Spike, THP-1 and peripheral blood mononuclear cells (PBMCs) were
918 maintained at 37°C under 5% CO₂ in RPMI media, supplemented with 10% FBS and 100 U/mL
919 penicillin/ streptomycin. 293T (or HEK293T), 293T-ACE2, CF2Th, TZM-bl and TZM-bl-ACE2 cells
920 were maintained at 37°C under 5% CO₂ in DMEM media, supplemented with 5% FBS and 100
921 U/mL penicillin/ streptomycin. CEM.NKr (NIH AIDS Reagent Program) is a T lymphocytic cell line
922 resistant to NK cell-mediated lysis. CEM.NKr-Spike stably expressing SARS-CoV-2 Spike were
923 used as target cells in ADCC and ADCP assays (Anand et al., 2021a). THP-1 monocytic cell line
924 (ATCC) was used as effector cells in the ADCP assay. PBMCs were obtained from healthy donor
925 through leukapheresis and were used as effector cells in ADCC assay. 293T cells (obtained from
926 ATCC) were derived from 293 cells, into which the simian virus 40 T-antigen was inserted. 293T-
927 ACE2 cells stably expressing human ACE2 is derived from 293T cells (Prevost et al., 2020).
928 Cf2Th cells (obtained from ATCC) are SARS-CoV-2-resistant canine thymocytes and were used
929 in the virus capture assay. TZM-bl (NIH AIDS Reagent Program) were derived from HeLa cells
930 and were engineered to contain the Tat-responsive firefly luciferase reporter gene. For the
931 generation of TZM-bl cells stably expressing human ACE2, transgenic lentiviruses were produced
932 in 293T using a third-generation lentiviral vector system. Briefly, 293T cells were co-transfected
933 with two packaging plasmids (pLP1 and pLP2), an envelope plasmid (pSVCMV-IN-VSV-G) and
934 a lentiviral transfer plasmid coding for human ACE2 (pLenti-C-mGFP-P2A-Puro-ACE2)
935 (OriGene). Forty-eight hours post-transfection, supernatant containing lentiviral particles was
936 used to infect TZM-bl cells in presence of 5 µg/mL of polybrene. Stably transduced cells were
937 enriched upon puromycin selection. TZM-bl-ACE2 cells were then cultured in medium
938 supplemented with 2 mg/mL of puromycin (Millipore Sigma).

939

940 **Ethics statement**

941 PBMCs from healthy individuals as a source of effector cells in our ADCC assay were obtained
942 under CRCHUM institutional review board (protocol #19.381). Research adhered to the standards
943 indicated by the Declaration of Helsinki. All participants were adults and provided informed written
944 consent prior to enrollment in accordance with Institutional Review Board approval.

945

946 **Antibodies**

947 The human antibodies (CV3-1 and CV3-25) used in the work were isolated from blood of male
948 convalescent donor S006 (male) recovered 41 days after symptoms onset using fluorescent
949 recombinant stabilized Spike ectodomains (S2P) as probes to identify antigen-specific B cells as
950 previously described (Lu et al., 2020; Seydoux et al., 2020). Site-directed mutagenesis was

951 performed on plasmids expressing CV3-1 and CV3-25 antibody heavy chains in order to introduce
952 the LALA mutations (L234A/L235A) using to the QuikChange II XL site-directed mutagenesis
953 protocol (Stratagene).

954

955 **Mouse Experiments**

956 All experiments were approved by the Institutional Animal Care and Use Committees (IACUC) of
957 and Institutional Biosafety Committee of Yale University (IBSCYU). All the animals were housed
958 under specific pathogen-free conditions in the facilities provided and supported by Yale Animal
959 Resources Center (YARC). All IVIS imaging, blood draw and virus inoculation experiments were
960 done under anesthesia using regulated flow of isoflurane:oxygen mix to minimize pain and
961 discomfort to the animals.

962 C57BL/6 (B6), hACE2 transgenic B6 mice (heterozygous) were obtained from Jackson
963 Laboratory. 6–8-week-old male and female mice were used for all the experiments. The
964 heterozygous mice were crossed and genotyped to select heterozygous mice for experiments by
965 using the primer sets recommended by Jackson Laboratory.

966

967 **METHOD DETAILS**

968

969 **SARS-CoV-2 infection and treatment conditions**

970 For all *in vivo* experiments, the 6 to 8 weeks male and female mice were intranasally challenged
971 with 1×10^5 FFU in 25-30 μl volume under anesthesia (0.5 - 5 % isoflurane delivered using
972 precision Dräger vaporizer with oxygen flow rate of 1 L/min). For NAb treatment using prophylaxis
973 regimen, mice were treated with 250 μg (12.5 mg/kg body weight) of indicated antibodies (CV3-1
974 or CV3-25) or in combination (1:1; 6.25 mg/kg body weight of each) via intraperitoneal injection
975 (i.p.) 24 h prior to infection. For mAb treatment under therapeutic regimen, mice were treated at
976 1, 3 and 4 dpi intraperitoneally with CV3-1(12.5 mg/kg body weight). Body weight was measured
977 and recorded daily. The starting body weight was set to 100 %. For survival experiments, mice
978 were monitored every 6-12 h starting six days after virus administration. Lethargic and moribund
979 mice or mice that had lost more than 20% of their body weight were sacrificed and considered to
980 have succumbed to infection for Kaplan-Meier survival plots.

981

982 **Bioluminescence Imaging (BLI) of SARS-CoV-2 infection**

983 All standard operating procedures and protocols for IVIS imaging of SARS-CoV-2 infected
984 animals under ABSL-3 conditions were approved by IACUC, IBSCYU and YARC. All the imaging

985 was carried out using IVIS Spectrum® (PerkinElmer) in XIC-3 animal isolation chamber
986 (PerkinElmer) that provided biological isolation of anesthetized mice or individual organs during
987 the imaging procedure. All mice were anesthetized via isoflurane inhalation (3 - 5 % isoflurane,
988 oxygen flow rate of 1.5 L/min) prior and during BLI using the XGI-8 Gas Anesthesia System. Prior
989 to imaging, 100 µL of nanoluciferase substrate, furimazine (NanoGlo™, Promega, Madison, WI)
990 diluted 1:40 in endotoxin-free PBS was retroorbitally administered to mice under anesthesia. The
991 mice were then placed into XIC-3 animal isolation chamber (PerkinElmer) pre-saturated with
992 isothesia and oxygen mix. The mice were imaged in both dorsal and ventral position at indicated
993 days post infection. The animals were then imaged again after euthanasia and necropsy by
994 spreading additional 200 µL of substrate on to exposed intact organs. Infected areas of interest
995 identified by carrying out whole-body imaging after necropsy were isolated, washed in PBS to
996 remove residual blood and placed onto a clear plastic plate. Additional droplets of furimazine in
997 PBS (1:40) were added to organs and soaked in substrate for 1-2 min before BLI.

998 Images were acquired and analyzed with the manufacturer's Living Image v4.7.3 *in vivo*
999 software package. Image acquisition exposures were set to auto, with imaging parameter
1000 preferences set in order of exposure time, binning, and f/stop, respectively. Images were acquired
1001 with luminescent f/stop of 2, photographic f/stop of 8. Binning was set to medium. Comparative
1002 images were compiled and batch-processed using the image browser with collective luminescent
1003 scales. Photon flux was measured as luminescent radiance (p/sec/cm²/sr). During luminescent
1004 threshold selection for image display, luminescent signals were regarded as background when
1005 minimum threshold levels resulted in displayed radiance above non-tissue-containing or known
1006 uninfected regions. To determine the pattern of virus spread, the image sequences were acquired
1007 every day following administration of SARS-CoV-2 (i.n). Image sequences were assembled and
1008 converted to videos using Image J.

1009

1010 **Biodistribution of therapeutic neutralizing antibodies using IVIS**

1011 Mice were intraperitoneally (i.p) administered with 250 µg of unconjugated (12.5 mg/kg body
1012 weight), Alexa Fluor 647 or Alexa Fluor 594-labeled antibodies to non-infected or SARS-CoV-2
1013 infected hACE2 mice. 24 h later all organs (nose, trachea, lung, cervical lymph nodes, brain, liver,
1014 spleen, kidney, gut, testis and seminal vesicles) were isolated after necropsy and images were
1015 acquired with an IVIS Spectrum® (PerkinElmer) and fluorescence radiance intensities were
1016 analyzed with the manufacturer's Living Image v4.7.3 *in vivo* software package. Organs were cut
1017 into half and weighed. One half was fixed in 4 % PFA and processed for cryoimmunohistology.

1018 The other half was resuspended in serum-free RPMI and homogenized in a bead beater for
1019 determination of antibody levels using quantitative ELISA.

1020

1021 **Measurement of therapeutic antibody levels in organs by quantitative ELISA**

1022 Recombinant SARS-CoV-2 RBD and S-6P proteins were used to quantify CV3-1 and CV3-25
1023 antibody levels, respectively, in mice organs. SARS-CoV-2 proteins (2.5 µg/ml), or bovine serum
1024 albumin (BSA) (2.5 µg/ml) as a negative control, were prepared in PBS and were adsorbed to
1025 plates (MaxiSorp; Nunc) overnight at 4 °C. Coated wells were subsequently blocked with blocking
1026 buffer (Tris-buffered saline [TBS], 0.1% Tween20, 2% BSA) for 1 hour at room temperature. Wells
1027 were then washed four times with washing buffer (TBS 0.1% Tween20). Titrated concentrations
1028 of CV3-1 or CV3-25 or serial dilutions of mice organ homogenates were prepared in a diluted
1029 solution of blocking buffer (0.1 % BSA) and incubated in wells for 90 minutes at room temperature.
1030 Plates were washed four times with washing buffer followed by incubation with HRP-conjugated
1031 anti-IgG secondary Abs (Invitrogen) (diluted in a diluted solution of blocking buffer [0.4% BSA])
1032 for 1 hour at room temperature, followed by four washes. HRP enzyme activity was determined
1033 after the addition of a 1:1 mix of Western Lightning oxidizing and luminol reagents (Perkin Elmer
1034 Life Sciences). Light emission was measured with a LB941 TriStar luminometer (Berthold
1035 Technologies). Signal obtained with BSA was subtracted for each organ. Titrated concentrations
1036 of CV3-1 or CV3-25 were used to establish a standard curve of known antibody concentrations
1037 and the linear portion of the curve was used to infer the antibody concentration in tested organ
1038 homogenates.

1039

1040 **Cryo-immunohistology of organs**

1041 Organs were isolated after necropsy and fixed in 1X PBS containing freshly prepared 4% PFA for
1042 12 h at 4 °C. They were then washed with PBS, cryoprotected with 10, 20 and 30% ascending
1043 sucrose series, snap-frozen in Tissue-Tek® O.C.T.™ compound and stored at -80 °C. The nasal
1044 cavity was snap-frozen in 8% gelatin prepared in 1X PBS and stored at -80 °C. 10 - 30 µm thick
1045 frozen sections were permeabilized with Triton X-100 and treated with Fc receptor blocker
1046 (Innovex Biosciences) before staining with indicated conjugated primary, secondary antibodies or
1047 Phalloidin in PBS containing 2 % BSA containing 10 % fetal bovine serum. Stained sections were
1048 treated with TrueVIEW Autofluorescence Quenching Kit (Vector Laboratories) and mounted in
1049 VECTASHIELD® Vibrance™ Antifade Mounting Medium. Images were acquired using Nikon W1
1050 spinning disk confocal microscope equipped with 405, 488, 561 and 647 nm laser lines. The
1051 images were processed using Nikon Elements AR version 4.5 software (Nikon Instruments Inc,

1052 Americas) and figures assembled with Photoshop CC and Illustrator CC (Adobe Systems, San
1053 Jose, CA, USA).

1054

1055 **Focus forming assay**

1056 Titers of virus stocks was determined by standard plaque assay. Briefly, the 4×10^5 Vero-E6 cells
1057 were seeded on 12-well plate. 24 h later, the cells were infected with 200 μL of serially diluted
1058 virus stock. After 1 hour, the cells were overlayed with 1ml of pre-warmed 0.6% Avicel (RC-581
1059 FMC BioPolymer) made in complete RPMI medium. Plaques were resolved at 48 h post infection
1060 by fixing in 10 % paraformaldehyde for 15 min followed by staining for 1 hour with 0.2 % crystal
1061 violet made in 20 % ethanol. Plates were rinsed in water to visualize plaques.

1062

1063 **Measurement of viral burden**

1064 Indicated organs (nasal cavity, brain, lungs from infected or uninfected mice were collected,
1065 weighed, and homogenized in 1 mL of serum free RPMI media containing penicillin-streptomycin
1066 and homogenized in 2 mL tube containing 1.5 mm Zirconium beads with BeadBug 6 homogenizer
1067 (Benchmark Scientific, TEquipment Inc). Virus titers were measured using three highly correlative
1068 methods. First, the total RNA was extracted from homogenized tissues using RNeasy plus Mini
1069 kit (Qiagen Cat # 74136), reverse transcribed with iScript advanced cDNA kit (Bio-Rad Cat
1070 #1725036) followed by a SYBR Green Real-time PCR assay for determining copies of SARS-
1071 CoV-2 N gene RNA using primers SARS-CoV-2 N F: 5'-ATGCTGCAATCGTGCTACAA-3' and
1072 SARS-CoV-2 N R: 5'-GACTGCCGCCTCTGCTC-3'.

1073 Second, serially diluted clarified tissue homogenates were used to infect Vero-E6 cell culture
1074 monolayer. The titers per gram of tissue were quantified using standard plaque forming assay
1075 described above. Third, we used nanoluciferase activity as a shorter surrogate for plaque assay.
1076 Infected cells were washed with PBS and then lysed using 1X Passive lysis buffer. The lysates
1077 transferred into a 96-well solid white plate (Costar Inc) and nanoluciferase activity was measured
1078 using Tristar multiwell Luminometer (Berthold Technology, Bad Wildbad, Germany) for 2.5
1079 seconds by adding 20 μl of Nano-Glo® substrate in nanoluc assay buffer (Promega Inc, WI, USA).
1080 Uninfected monolayer of Vero cells treated identically served as controls to determine basal
1081 luciferase activity to obtain normalized relative light units. The data were processed and plotted
1082 using GraphPad Prism 8 v8.4.3.

1083

1084 **Analyses of signature inflammatory cytokines mRNA**

1085 Brain and lung samples were collected from mice at the time of necropsy. Approximately, 20 mg
1086 of tissue was suspended in 500 μ L of RLT lysis buffer, and RNA was extracted using RNeasy
1087 plus Mini kit (Qiagen Cat # 74136), reverse transcribed with iScript advanced cDNA kit (Bio-Rad
1088 Cat #1725036). To determine levels of signature inflammatory cytokines, multiplex qPCR was
1089 conducted using iQ Multiplex Powermix (Bio Rad Cat # 1725848) and PrimePCR Probe Assay
1090 mouse primers FAM-GAPDH, HEX-IL6, TEX615-CCL2, Cy5-CXCL10, and Cy5.5-IFNgamma.
1091 The reaction plate was analyzed using CFX96 touch real time PCR detection system. Scan mode
1092 was set to all channels. The PCR conditions were 95 °C 2 min, 40 cycles of 95 °C for 10 s and
1093 60 °C for 45 s, followed by a melting curve analysis to ensure that each primer pair resulted in
1094 amplification of a single PCR product. mRNA levels of *Il6*, *Ccl2*, *Cxcl10* and *Ifng* in the cDNA
1095 samples of infected mice were normalized to *Gapdh* with the formula $\Delta C_t(\text{target gene}) = C_t(\text{target}$
1096 $\text{gene}) - C_t(\text{Gapdh})$. The fold increase was determined using $2^{-\Delta\Delta C_t}$ method comparing treated mice
1097 to uninfected controls.

1098

1099 **Antibody depletion of immune cell subsets**

1100 For evaluating the effect of NK cell depletion during CV3-1 prophylaxis, anti-NK1.1 (clone PK136;
1101 12.5 mg/kg body weight) or an isotype control mAb (BioXCell; clone C1.18.4; 12.5 mg/kg body
1102 weight) was administered to mice by i.p. injections every 2 days starting at 48 h before SARS-
1103 CoV-2-nLuc challenge till 8 dpi. The mice were bled after two days of antibody depletion, necropsy
1104 or at 10 dpi (surviving mice) for analyses. To evaluate the effect of NK cell and neutrophil depletion
1105 during CV3-1 therapy, anti-NK1.1 (clone PK136; 12.5 mg/kg body weight) or anti-Ly6G (clone:
1106 1A8; 12.5 mg/kg body weight) was administered to mice by i.p injection every two days starting
1107 at 1 dpi respectively. Rat IgG2a mAb (BioXCell; clone C1.18.4; 12.5 mg/kg body weight) was
1108 used as isotype control. The mice were sacrificed and bled at 10 dpi for analyses. For evaluating
1109 the effect of monocyte depletion on CV3-1 therapy, anti-CCR2 (clone MC-21; 2.5 mg/kg body
1110 weight) (Mack et al., 2001) or an isotype control mAb (BioXCell; clone LTF-2; 2.5 mg/kg body
1111 weight) was administered to mice by i.p injection every two days starting at 1 dpi. The mice were
1112 sacrificed and bled 2-3 days after antibody administration or at 10 dpi to ascertain depletion of
1113 desired population.

1114

1115 **Flow Cytometric Analyses**

1116 For analysis of immune cell depletion, peripheral blood was collected before infection and on day
1117 of harvest. Erythrocytes were lysed with RBC lysis buffer (BioLegend Inc), PBMCs fixed with 4 %
1118 PFA and quenched with PBS containing 0.1M glycine. PFA-fixed cells PBMCs were resuspended

1119 and blocked in Cell Staining buffer (BioLegend Inc.) containing Fc blocking antibody against
1120 CD16/CD32 (BioLegend Inc) before staining with antibodies. NK cells were identified as CD3-
1121 NK1.1+ cells using PE/Cy7 anti-mouse CD3(17A2) and APC anti-mouse NK-1.1 (PK136).
1122 Neutrophils were identified as CD45+CD11b+Ly6G+ cells using APC Rat anti-mouse CD45 (30-
1123 F11), PE anti-mouse CD11b (M1/70) APC/Cy7 and anti-mouse Ly-6G (1A8). Ly6C^{hi} monocytes
1124 were identified as CD45⁺CD11b⁺Ly6C^{hi} cells using APC Rat anti-mouse CD45 (30-F11), PE anti-
1125 mouse CD11b (M1/70) and APC/Cy7 anti-mouse Ly-6C (HK1.4). Data were acquired on an Accuri
1126 C6 (BD Biosciences) and were analyzed with Accuri C6 software. FlowJo software (Treestar) was
1127 used to generate FACS plot shown in Figure S7. 100,000 – 200,000 viable cells were acquired
1128 for each sample.

1129

1130 **Sample Preparation for Electron Microscopy**

1131 Lung, brain and testis tissue samples from hACE2 transgenic mice challenged intranasally with
1132 SARS-CoV-2-nLuc (1×10^5 FFU; 6 dpi) were imaged after necropsy using bioluminescence
1133 imaging (IVIS, Perkin Elmer), pruned to isolate regions with high nLuc activity and immediately
1134 pre-fixed with 3 % glutaraldehyde, 1 % paraformaldehyde, 5 % sucrose in 0.1 M sodium
1135 cacodylate trihydrate to render them safe for handling outside of BSL3 containment. Viral
1136 infections of cultured cells were conducted at the UVM BSL-3 facility using an approved
1137 Institutional Biosafety protocol. SARS-CoV-2 strain 2019-nCoV/USA_USA-WA1/2020 (WA1;
1138 generously provided by K. Plante, World Reference Center for Emerging Viruses and
1139 Arboviruses, University of Texas Medical Branch) and propagated in African green monkey kidney
1140 (Vero E6) cells. Vero E6 cells were maintained in complete Dulbecco's Modified Eagle Medium
1141 (DMEM; Thermo Fisher, Cat. #11965–092) containing 10% fetal bovine serum (Gibco, Thermo-
1142 Fisher, Cat. #16140–071), 1% HEPES Buffer Solution (15630–130), and 1 % penicillin–
1143 streptomycin (Thermo Fisher, Cat. #15140–122). Cells were grown in a humidified incubator at
1144 37 °C with 5 % CO₂. Vero E6 cells were seeded into six well dishes and infected with SARS-CoV-
1145 2 at a multiplicity of infection of 0.01 for 48 hours before fixing and preparing for electron
1146 microscopy. Cells were pre-fixed with 3% glutaraldehyde, 1% paraformaldehyde, 5 % sucrose in
1147 0.1M sodium cacodylate trihydrate, removed from the plates and further prepared by high-
1148 pressure freezing and freeze-substitution as described below.
1149 Tissues samples were further cut to ~0.5 mm³ blocks and cultured cells were gently pelleted.
1150 Both samples were rinsed with fresh cacodylate buffer and placed into brass planchettes (Type
1151 A; Ted Pella, Inc., Redding, CA) prefilled with 10 % Ficoll in cacodylate buffer. The tissues were
1152 covered with the flat side of a Type-B brass planchette and rapidly frozen with an HPM-010 high-

1153 pressure freezing machine (Leica Microsystems, Vienna Austria). The frozen samples were
1154 transferred under liquid nitrogen to cryotubes (Nunc) containing a frozen solution of 2.5 % osmium
1155 tetroxide, 0.05 % uranyl acetate in acetone. Tubes were loaded into an AFS-2 freeze-substitution
1156 machine (Leica Microsystems) and processed at -90°C for 72 h, warmed over 12 h to -20°C, held
1157 at that temperature for 6 h, then warmed to 4°C for 2 h. The fixative was removed, and the
1158 samples rinsed 4 x with cold acetone, following which they were infiltrated with Epon-Araldite
1159 resin (Electron Microscopy Sciences, Port Washington PA) over 48 h. The spleen tissue was flat-
1160 embedded between two Teflon-coated glass microscope slides. Resin was polymerized at 60°C
1161 for 48 h.

1162

1163 **Electron Microscopy and Dual-Axis Tomography**

1164 Flat-embedded tissue samples or portions of cell pellets were observed with a stereo dissecting
1165 microscope and appropriate regions were extracted with a microsurgical scalpel and glued to the
1166 tips of plastic sectioning stubs. Semi-thin (150-200 nm) serial sections were cut with a UC6
1167 ultramicrotome (Leica Microsystems) using a diamond knife (Diatome, Ltd. Switzerland). Sections
1168 were placed on formvar-coated copper-rhodium slot grids (Electron Microscopy Sciences) and
1169 stained with 3 % uranyl acetate and lead citrate. Gold beads (10 nm) were placed on both surfaces
1170 of the grid to serve as fiducial markers for subsequent image alignment. Sections were placed in
1171 a dual-axis tomography holder (Model 2040, E.A. Fischione Instruments, Export PA) and imaged
1172 with a Tecnai T12-G2 transmission electron microscope operating at 120 KeV (ThermoFisher
1173 Scientific) equipped with a 2k x 2k CCD camera (XP1000; Gatan, Inc. Pleasanton CA).
1174 Tomographic tilt-series and large-area montaged overviews were acquired automatically using
1175 the SerialEM software package (Mastronarde, 2005, 2008; Mastronarde and Held, 2017). For
1176 tomography, samples were tilted +/- 62° and images collected at 1° intervals. The grid was then
1177 rotated 90° and a similar series taken about the orthogonal axis. Tomographic data was
1178 calculated, analyzed, and modeled using the IMOD software package (Mastronarde, 2005, 2008;
1179 Mastronarde and Held, 2017) on iMac Pro and MacPro computers (Apple, Inc., Cupertino, CA).
1180 Montaged projection overviews were used to illustrate spatial perspective, identify cell types and
1181 frequency within the tissue sections. High-resolution 3D electron tomography was used to confirm
1182 virus particles and characterize virus-containing compartments within infected cells.

1183

1184 **Identification and Characterization of SARS-CoV-2 Virions in infected cells and tissues.**

1185 Particles resembling virions were examined in 3D by tomography to determine their identity.
1186 Presumptive SARS-CoV-2 virions were identified from tomographic reconstructions of tissue

1187 samples by observing structures resembling virions described in cryo-electron tomography
1188 studies of purified SARS-CoV-2 and of SARS-CoV-2 in infected cells (Ke et al., 2020; Klein et al.,
1189 2020; Turonova et al., 2020; Yao et al., 2020). These were compared to identified virions within
1190 SARS-CoV-2-infected cultured Vero E6 cells that had been prepared for EM by the same
1191 methodology (Figure 2O-Q). We used the following criteria to positively identify SARS-CoV-2
1192 virions in tissues: (i) Structures that were spherical in 3D with ~60-120 nm diameters and were
1193 not continuous with other adjacent structures, (ii) Spherical structures with densities
1194 corresponding to a distinct membrane bilayer, internal puncta consistent with ribonucleoproteins
1195 (Yao et al., 2020), and densities corresponding to surface spikes on the external peripheries of
1196 the spheres. In further characterization of virions, we noted that the inner vesicles of multivesicular
1197 bodies (MVBs) have been mis-identified as SARS-CoV-2 by electron microscopy (Calomeni et
1198 al., 2020). We therefore compared measurements of MVB inner vesicles and presumptive
1199 coronavirus virions from what we identified as intracellular exit compartments within the same
1200 tomogram (data not shown) with our previous tomographic reconstructions of MVBs (He et al.,
1201 2008; Ladinsky et al., 2012). We distinguished virions inside of cytoplasmic exit compartments
1202 from the inner vesicles of MVBs based on differences in size (MVB inner virions are generally
1203 smaller in diameter than coronaviruses) and the presence of surface spikes and internal puncta
1204 (MVB inner vesicles do not present surface spikes or internal puncta).

1205 **Immunoelectron microscopy.**

1206 SARS-CoV-2 infected tissues were extracted and immediately fixed with 4% paraformaldehyde,
1207 5% sucrose in 0.1M cacodylate buffer. Tissues were cut into ~0.5 mm³ pieces and infiltrated into
1208 2.1M sucrose in 0.1M cacodylate buffer for 24 h. Individual tissue pieces were placed onto
1209 aluminum cryosectioning stubs (Ted Pella, Inc.) and rapidly frozen in liquid nitrogen. Thin (100
1210 nm) cryosections were cut with a UC6/FC6 cryoultramicrotome (Leica Microsystems) using a
1211 cryo-diamond knife (Diatome, Ltd., Switzerland) at -110°C. Sections were picked up with a wire
1212 loop in a drop of 2.3M sucrose in 0.1M cacodylate buffer and transferred to Formvar-coated,
1213 carbon-coated, glow-discharged 100-mesh copper/rhodium grids (Electron Microscopy
1214 Sciences). Grids were incubated 1 hr with 10% calf serum in PBS to block nonspecific antibody
1215 binding, then incubated 2 hrs with anti-S antiserum (Cohen et al., 2021). Mosaic nanoparticles
1216 elicit cross-reactive immune responses to zoonotic coronaviruses in mice (Cohen et al., 2021).
1217 diluted 1:500 in PBS with 5% calf serum. Grids were rinsed (4x 10') with PBS then labeled for 2
1218 hrs with 10 nm gold conjugated goat anti-mouse secondary antibody (Ted Pella, Inc.). Grids were
1219 again rinsed (4x 10') with PBS, then 3x with distilled water and negatively stained with 1% uranyl

1220 acetate in 1% methylcellulose (Sigma) for 20'. Grids were air-dried in wire loops and imaged as
1221 described for ET.

1222

1223 **Protein expression and purification**

1224 FreeStyle 293F cells (Thermo Fisher Scientific) were grown in FreeStyle 293F medium (Thermo
1225 Fisher Scientific) to a density of 1x10⁶ cells/mL at 37°C with 8% CO₂ with regular agitation (150
1226 rpm). Cells were transfected with a plasmid coding for recombinant stabilized SARS-CoV-2
1227 ectodomain (S-6P; obtained from Dr. Jason S. McLellan) or SARS-CoV-2 RBD (Beaudoin-
1228 Bussieres et al., 2020) using ExpiFectamine 293 transfection reagent, as directed by the
1229 manufacturer (Thermo Fisher Scientific). One-week post-transfection, supernatants were clarified
1230 and filtered using a 0.22 µm filter (Thermo Fisher Scientific). The recombinant S-6P was purified
1231 by strep-tactin resin (IBA) following by size-exclusion chromatography on Superose 6 10/300
1232 column (GE Healthcare) in 10 mM Tris pH 8.0 and 200 mM NaCl (SEC buffer). RBD was purified
1233 by Ni-NTA column (Invitrogen) and gel filtration on Hiload 16/600 Superdex 200pg using the same
1234 SEC buffer. Purified proteins were snap-frozen at liquid nitrogen and stored in aliquots at 80°C
1235 until further use. Protein purities were confirmed as one single-band on SDS-PAGE.

1236

1237 **SARS-CoV-2 Spike ELISA (enzyme-linked immunosorbent assay)**

1238 The SARS-CoV-2 Spike ELISA assay used was recently described (Beaudoin-Bussieres et al.,
1239 2020; Prevost et al., 2020). Briefly, recombinant SARS-CoV-2 S-6P and RBD proteins (2.5 µg/ml),
1240 or bovine serum albumin (BSA) (2.5 µg/ml) as a negative control, were prepared in PBS and were
1241 adsorbed to plates (MaxiSorp; Nunc) overnight at 4 °C. Coated wells were subsequently blocked
1242 with blocking buffer (Tris-buffered saline [TBS] containing 0.1% Tween20 and 2% BSA) for 1 hour
1243 at room temperature. Wells were then washed four times with washing buffer (TBS containing
1244 0.1% Tween20). CV3-1, CV3-25 and CR3022 mAbs (50 ng/ml) were prepared in a diluted solution
1245 of blocking buffer (0.1 % BSA) and incubated with the RBD-coated wells for 90 minutes at room
1246 temperature. Plates were washed four times with washing buffer followed by incubation with HRP-
1247 conjugated anti-IgG secondary Abs (Invitrogen) (diluted in a diluted solution of blocking buffer
1248 [0.4% BSA]) for 1 hour at room temperature, followed by four washes. HRP enzyme activity was
1249 determined after the addition of a 1:1 mix of Western Lightning oxidizing and luminol reagents
1250 (Perkin Elmer Life Sciences). Light emission was measured with a LB941 TriStar luminometer
1251 (Berthold Technologies). Signal obtained with BSA was subtracted for each plasma and was then
1252 normalized to the signal obtained with CR3022 mAb present in each plate.

1253

1254 **Flow cytometry analysis of cell-surface Spike staining.**

1255 Spike expressors of human coronaviruses SARS-CoV-2, SARS-CoV-1, MERS-CoV, OC43, NL63
1256 and 229E were reported elsewhere (Hoffmann et al., 2020; Hoffmann et al., 2013; Hofmann et
1257 al., 2005; Park et al., 2016; Prevost et al., 2020). Expressors of HKU1 Spike and SARS-CoV-2
1258 S2 N-His were purchased from Sino Biological. Using the standard calcium phosphate method,
1259 10 µg of Spike expressor and 2 µg of a green fluorescent protein (GFP) expressor (pIRES2-
1260 eGFP) was transfected into 2×10^6 293T cells. At 48 hours post transfection, 293T cells were
1261 stained with CV3-1 and CV3-25 antibodies (5µg/mL), using cross-reactive anti-SARS-CoV-1
1262 Spike CR3022 or mouse anti-His tag (Sigma-Aldrich) as positive controls. Alexa Fluor-647-
1263 conjugated goat anti-human IgG (H+L) Abs (Invitrogen) and goat anti-mouse IgG (H+L) Abs
1264 (Invitrogen) were used as secondary antibodies. The percentage of transfected cells (GFP+ cells)
1265 was determined by gating the living cell population based on the basis of viability dye staining
1266 (Aqua Vivid, Invitrogen). Samples were acquired on a LSRII cytometer (BD Biosciences) and data
1267 analysis was performed using FlowJo v10 (Tree Star).

1268

1269 **Virus capture assay**

1270 The SARS-CoV-2 virus capture assay was previously reported (Ding et al., 2020). Briefly,
1271 pseudoviral particles were produced by transfecting 2×10^6 HEK293T cells with pNL4.3 Luc R-E-
1272 (3.5 µg), plasmids encoding for SARS-CoV-2 Spike or SARS-CoV-1 Spike (3.5 µg) protein and
1273 VSV-G (pSVCMV-IN-VSV-G, 1 µg) using the standard calcium phosphate method. Forty-eight
1274 hours later, supernatant-containing virion was collected, and cell debris was removed through
1275 centrifugation (1,500 rpm for 10 min). To immobilize antibodies on ELISA plates, white MaxiSorp
1276 ELISA plates (Thermo Fisher Scientific) were incubated with 5 µg/ml of antibodies in 100 µl
1277 phosphate-buffered saline (PBS) overnight at 4°C. Unbound antibodies were removed by
1278 washing the plates twice with PBS. Plates were subsequently blocked with 3% bovine serum
1279 albumin (BSA) in PBS for 1 hour at room temperature. After two washes with PBS, 200 µl of virus-
1280 containing supernatant was added to the wells. After 4 to 6 hours incubation, supernatants were
1281 removed and the wells were washed with PBS 3 times. Virus capture by any given antibody was
1282 visualized by adding 1×10^4 SARS-CoV-2-resistant Cf2Th cells per well in complete DMEM
1283 medium. Forty-eight hours post-infection, cells were lysed by the addition of 30 µL of passive lysis
1284 buffer (Promega) and three freeze-thaw cycles. An LB941 TriStar luminometer (Berthold
1285 Technologies) was used to measure the luciferase activity of each well after the addition of 100
1286 µL of luciferin buffer (15 mM MgSO₄, 15 mM KH₂PO₄ [pH 7.8], 1 mM ATP, and 1 mM dithiothreitol)
1287 and 50 µL of 1 mM D-luciferin potassium salt (ThermoFisher Scientific).

1288 **Surface plasmon resonance (SPR)**

1289 All surface plasma resonance assays were performed on a Biacore 3000 (GE Healthcare) with a
1290 running buffer of 10 mM HEPES pH 7.5 and 150 mM NaCl, supplemented with 0.05% Tween 20
1291 at 25°C. The binding affinity and kinetics to the SARS-CoV-2 spike (S) trimer (SARS-CoV-2 S
1292 HexaPro [S-6P]) (Hsieh et al., 2020) and SARS-CoV-2 S2 ectodomain (baculovirus produced his-
1293 tagged S2(686-1213) from BEI Resources (NR-53799) were evaluated using monovalent CV3-1
1294 and CV3-25 Fab. Fabs were generated by standard papain digestion (Thermo Fisher) and purified
1295 by Protein A affinity chromatography and gel filtration. His-tagged SARS-CoV-2 S-6P or SARS-
1296 CoV-2 S2 ectodomain was immobilized onto a Ni-NTA sensor chip at a level of ~1000 and ~630
1297 RU response units (RUs), respectively. Two-fold serial dilutions of CV3-1 or CV3-25 Fab were
1298 injected in a concentration range of 1.56-100 nM over the SARS-CoV-2 S-6P and CV3-25 Fab in
1299 a range of 3.125 to 200 to nM over the SARS-CoV-2 S2. After each cycle the Ni-NTA sensor chip
1300 was regenerated with a wash step of 0.1 M EDTA and reloaded with 0.1 M nickel sulfate followed
1301 by the immobilization of fresh antigens for the next cycle. The binding kinetics of SARS-CoV-2
1302 RBD and CV3-1 were obtained in a format where CV3-1 IgG was immobilized onto a Protein A
1303 sensor chip (Cytiva) with ~300 (RUs) and serial dilutions of SARS-CoV-2 RBD were injected with
1304 concentrations ranging from 1.56 to 50 nM. The protein A chip was regenerated with a wash step
1305 of 0.1 M glycine pH 2.0 and reloaded with IgG after each cycle.

1306 All sensograms were corrected by subtraction of the corresponding blank channel and the kinetic
1307 constant determined using a 1:1 Langmuir model with the BIA evaluation software (GE
1308 Healthcare). Goodness of fit of the curve was evaluated by the Chi² value with a value below 3
1309 considered acceptable

1310

1311 **Pseudovirus neutralization assay**

1312 Target cells were infected with single-round luciferase-expressing lentiviral particles. Briefly, 293T
1313 cells were transfected by the calcium phosphate method with the pNL4.3 R-E- Luc plasmid (NIH
1314 AIDS Reagent Program) and a plasmid encoding for SARS-CoV-2 Spike at a ratio of 5:4. Two
1315 days post-transfection, cell supernatants were harvested and stored at -80°C until use. 293T-
1316 ACE2 (Prevost et al., 2020) target cells were seeded at a density of 1×10^4 cells/well in 96-well
1317 luminometer-compatible tissue culture plates (Perkin Elmer) 24 h before infection. Recombinant
1318 viruses in a final volume of 100 µL were incubated with the indicated semi-log diluted antibody
1319 concentrations for 1 h at 37°C and were then added to the target cells followed by incubation for
1320 48 h at 37°C; cells were lysed by the addition of 30 µL of passive lysis buffer (Promega) followed
1321 by one freeze-thaw cycle. An LB941 TriStar luminometer (Berthold Technologies) was used to

1322 measure the luciferase activity of each well after the addition of 100 µL of luciferin buffer (15 mM
1323 MgSO₄, 15 mM KH₂PO₄ [pH 7.8], 1 mM ATP, and 1 mM dithiothreitol) and 50 µL of 1 mM d-
1324 luciferin potassium salt. The neutralization half-maximal inhibitory dilution (IC₅₀) represents the
1325 plasma dilution to inhibit 50 % of the infection of 293T-ACE2 cells by recombinant viruses bearing
1326 the SARS-CoV-2 S glycoproteins.

1327

1328 **Microneutralization assay**

1329 A microneutralization assay for SARS-CoV-2 serology was performed as previously described
1330 (Amanat et al., 2020). Experiments were conducted with the SARS-CoV-2 USA-WA1/2020 virus
1331 strain (obtained from BEI resources). One day prior to infection, 2x10⁴ Vero E6 cells were seeded
1332 per well of a 96 well flat bottom plate and incubated overnight at 37°C under 5% CO₂ to permit
1333 cell adherence. Titrated antibody concentrations were performed in a separate 96 well culture
1334 plate using MEM supplemented with penicillin (100 U/mL), streptomycin (100 mg/mL), HEPES,
1335 L-Glutamine (0.3 mg/mL), 0.12% sodium bicarbonate, 2% FBS (all from Thermo Fisher Scientific)
1336 and 0.24% BSA (EMD Millipore Corporation). In a Biosafety Level 3 laboratory (ImPaKT Facility,
1337 Western University), 10³ TCID₅₀/mL of SARS-CoV-2 USA-WA1/2020 live virus was prepared in
1338 MEM + 2% FBS and combined with an equivalent volume of respective antibody dilutions for one
1339 hour at room temperature. After this incubation, all media was removed from the 96 well plate
1340 seeded with Vero E6 cells and virus:antibody mixtures were added to each respective well at a
1341 volume corresponding to 600 TCID₅₀ per well and incubated for one hour further at 37°C. Both
1342 virus only and media only (MEM + 2% FBS) conditions were included in this assay. All
1343 virus:plasma supernatants were removed from wells without disrupting the Vero E6 monolayer.
1344 Each antibody concentration (100 µL) was added to its respective Vero E6-seeded well in addition
1345 to an equivalent volume of MEM + 2% FBS and was then incubated for 48 hours. Media was then
1346 discarded and replaced with 10% formaldehyde for 24 hours to cross-link Vero E6 monolayer.
1347 Formaldehyde was removed from wells and subsequently washed with PBS. Cell monolayers
1348 were permeabilized for 15 minutes at room temperature with PBS + 0.1% Triton X-100, washed
1349 with PBS and then incubated for one hour at room temperature with PBS + 3% non-fat milk. An
1350 anti-mouse SARS-CoV-2 nucleocapsid protein (Clone 1C7, Bioss Antibodies) primary antibody
1351 solution was prepared at 1 mg/mL in PBS + 1% non-fat milk and added to all wells for one hour
1352 at room temperature. Following extensive washing with PBS, an anti-mouse IgG HRP secondary
1353 antibody solution was formulated in PBS + 1% non-fat milk. One-hour post-incubation, wells were
1354 washed with PBS, SIGMAFAST OPD developing solution (Millipore Sigma) was prepared as per
1355 manufacturer's instructions and added to each well for 12 minutes. Dilute HCl (3.0 M) was added

1356 to quench the reaction and the optical density at 490 nm of the culture plates was immediately
1357 measured using a Synergy LX multi-mode reader and Gen5 microplate reader and imager
1358 software (BioTek).

1359

1360 **Cell-to-cell fusion assay**

1361 To assess cell-to-cell fusion, 2×10^6 293T cells were co-transfected with plasmid expressing HIV-
1362 1 Tat (1 μ g) and a plasmid expressing SARS-CoV-2 Spike (4 μ g) using the calcium phosphate
1363 method. Two days after transfection, Spike-expressing 293T (effector cells) were detached with
1364 PBS-EDTA 1mM and incubated for 1 hour with indicated amounts of CV3-1 and/or CV3-25 NAbs
1365 at 37°C and 5% CO₂. Subsequently, effector cells (1×10^4) were added to TZM-bl-ACE2 target
1366 cells that were seeded at a density of 1×10^4 cells/well in 96-well luminometer-compatible tissue
1367 culture plates 24 h before the assay. Cells were co-incubated for 6 h at 37°C and 5% CO₂, after
1368 which they were lysed by the addition of 40 μ l of passive lysis buffer (Promega) and one freeze-
1369 thaw cycles. An LB 941 TriStar luminometer (Berthold Technologies) was used to measure the
1370 luciferase activity of each well after the addition of 100 μ l of luciferin buffer (15 mM MgSO₄, 15
1371 mM KH₂PO₄ [pH 7.8], 1 mM ATP, and 1 mM dithiothreitol) and 50 μ L of 1 mM d-luciferin potassium
1372 salt (ThermoFisher Scientific).

1373

1374 **Antibody dependent cellular cytotoxicity (ADCC) assay**

1375 For evaluation of anti-SARS-CoV-2 ADCC activity, parental CEM.NKr CCR5+ cells were mixed
1376 at a 1:1 ratio with CEM.NKr-Spike cells. These cells were stained for viability (AquaVivid; Thermo
1377 Fisher Scientific) and a cellular dye (cell proliferation dye eFluor670; Thermo Fisher Scientific)
1378 and subsequently used as target cells. Overnight rested PBMCs were stained with another
1379 cellular marker (cell proliferation dye eFluor450; Thermo Fisher Scientific) and used as effector
1380 cells. Stained effector and target cells were mixed at a 10:1 ratio in 96-well V-bottom plates.
1381 Titrated concentrations of CV3-1 and CV3-25 mAbs were added to the appropriate wells. The
1382 plates were subsequently centrifuged for 1 min at 300xg, and incubated at 37°C, 5% CO₂ for 5
1383 hours before being fixed in a 2% PBS-formaldehyde solution.

1384 ADCC activity was calculated using the formula: [(% of GFP+ cells in Targets plus Effectors)-(%
1385 of GFP+ cells in Targets plus Effectors plus antibody)]/(% of GFP+ cells in Targets) x 100 by
1386 gating on transduced live target cells. All samples were acquired on an LSRII cytometer (BD
1387 Biosciences) and data analysis performed using FlowJo v10 (Tree Star).

1388

1389 **Antibody dependent cellular phagocytosis (ADCP) assay**

1390 The ADCP assay was performed using CEM.NKr-Spike cells as target cells that were
1391 fluorescently labelled with a cellular dye (cell proliferation dye eFluor450). THP-1 cells were used
1392 as effector cells and were stained with another cellular dye (cell proliferation dye eFluor670).
1393 Stained target and effector cells were mixed at a 5:1 ratio in 96-well U-bottom plates. Titrated
1394 concentrations of CV3-1 and CV3-25 mAbs were added to the appropriate wells. After an
1395 overnight incubation at 37 °C and 5% CO₂, cells were fixed with a 2% PBS-formaldehyde solution.
1396 Antibody-mediated phagocytosis was determined by flow cytometry, gating on THP-1 cells that
1397 were double-positive for efluor450 and efluor670 cellular dyes. All samples were acquired on an
1398 LSRII cytometer (BD Biosciences) and data analysis performed using FlowJo v10 (Tree Star).

1399

1400 **smFRET imaging of S on SARS-CoV-2 VLPs (S-MEN particles)**

1401 S-MEN coronavirus-like particles carrying SARS-CoV-2 spikes were prepared similarly as
1402 previously described (Lu et al., 2020). The peptides tags-carrying spike plasmid (pCMV-S Q3-1
1403 A4-1: Q3 - GQQQLG; A4 - DSLDMLEM) was used to make S-MEN coronavirus-like particles.
1404 Plasmids encoding wildtype pCMV-S, dual-tagged pCMV-S Q3-1 A4-1, pLVX-M, pLVX-E, and
1405 pLVX-N were transfected into 293T cells at a ratio of 20:1:21:21:21. Using this very diluted ratio
1406 of tagged-S vs. wildtype S, the vast majority of S-MEN particles carry wildtype spikes. For the rest
1407 of the virus particles containing tagged S, more than 95 % S trimers will have one dual-tagged
1408 protomer and two wildtype protomers within a trimer. Using this strategy, we generated S-MEN
1409 particles with an average of one dual-tagged S protomer for conjugating FRET-paired
1410 fluorophores among predominantly wildtype S trimers presented on VLP surface. S-MEN particles
1411 were harvested 40 h post-transfection, filtered with a 0.45 µm pore size filter, and partially purified
1412 using ultra-centrifugation at 25,000 rpm for 2 h through a 15 % sucrose cushion made in PBS. S-
1413 MEN particles were then re-suspended in 50 mM pH 7.5 HEPES buffer, labeled with Cy3B(3S)
1414 and Cy5 derivative (LD650-CoA) and purified through an optiprep gradient as previously
1415 described (Lu et al., 2019; Lu et al., 2020; Munro et al., 2014)

1416 smFRET images of S-MEN particles was acquired on a home-built prism-based total internal
1417 reflection fluorescence (TIRF) microscope, as described previously (Lu et al., 2020). smFRET
1418 data analysis was performed using MATLAB (MathWorks)-based customized SPARTAN software
1419 package (Juette et al., 2016). The conformational effects of 50 ug/ml CV3-1 and CV3-25
1420 antibodies on SARS-CoV-2 spike were tested by pre-incubating fluorescently labeled viruses for
1421 60 mins at 37 °C before imaging in the continued presence of the antibodies. During smFRET
1422 imaging, fluorescently-labeled S-MEN particles were monitored for 80 seconds, where

1423 fluorescence from Cy3B(3S) and LD650-CoA labeled on S-MEN particles was recorded
1424 simultaneously at 25 frames per second for 80 seconds. Donor (Cy3B(3S)) and acceptor (LD650-
1425 CoA) fluorescence intensity traces were extracted after subtracting background signals and
1426 correcting cross-talks. The energy transfer efficiency (FRET) traces were generated from
1427 fluorescence intensity traces, according to $FRET = I_A / (\gamma I_D + I_A)$, where I_D and I_A are the fluorescence
1428 intensities of donor and acceptor, respectively, γ is the correlation coefficient compromising the
1429 discrepancy in quantum yields and detection efficiencies of two fluorophores. FRET is sensitive
1430 to changes in distances between the donor and the acceptor over time, ultimately translating into
1431 the conformational profiles and dynamics of S on S-MEN particles. S-MEN particles that contain
1432 incomplete FRET-paired fluorophores or more than one FRETing pairs of donor and acceptor on
1433 a single virus particle were automatically filtered from virus pools for further analysis. FRET traces
1434 of fluorescently-labeled S-MEN particles which meet the criteria of sufficient signal-to-noise ratio
1435 and anti-correlated fluctuations in donor and acceptor fluorescence intensity are indicative of live
1436 molecules. These FRET traces, indicated the number of traces in Figure 3, were then compiled
1437 into FRET histograms in Figure 3. Each FRET histogram was fitted into the sum of four Gaussian
1438 distributions in Matlab, where each Gaussian distribution represents one conformation and the
1439 area under each Gaussian curve estimates the occupancy.

1440

1441 **Quantification and Statistical Analysis**

1442 Data were analyzed and plotted using GraphPad Prism software (La Jolla, CA, USA). Statistical
1443 significance for pairwise comparisons were derived by applying non-parametric Mann-Whitney
1444 test (two-tailed). To obtain statistical significance for survival curves, grouped data were
1445 compared by log-rank (Mantel-Cox) test. To obtain statistical significance for grouped data we
1446 employed 2-way ANOVA followed by Dunnett's or Tukey's multiple comparison tests.

1447 p values lower than 0.05 were considered statistically significant. P values were indicated as *, p
1448 < 0.05; **, p < 0.01; ***, p < 0.001; ****, p < 0.0001.

1449

1450 **Schematics**

1451 Schematics for showing experimental design in figures were created with BioRender.com.

1453 **References**

- 1454 Alsoussi, W.B., Turner, J.S., Case, J.B., Zhao, H., Schmitz, A.J., Zhou, J.Q., Chen, R.E., Lei, T.,
1455 Rizk, A.A., McIntire, K.M., et al. (2020). A Potently Neutralizing Antibody Protects Mice against
1456 SARS-CoV-2 Infection. *J Immunol* 205, 915-922.
1457
- 1458 Amanat, F., White, K.M., Miorin, L., Strohmeier, S., McMahon, M., Meade, P., Liu, W.C., Albrecht,
1459 R.A., Simon, V., Martinez-Sobrido, L., et al. (2020). An In Vitro Microneutralization Assay for
1460 SARS-CoV-2 Serology and Drug Screening. *Curr Protoc Microbiol* 58, e108.
1461
- 1462 Anand, S.P., Prevost, J., Nayrac, M., Beaudoin-Bussieres, G., Benlarbi, M., Gasser, R., Brassard,
1463 N., Laumaea, A., Gong, S.Y., Bourassa, C., et al. (2021a). Longitudinal analysis of humoral
1464 immunity against SARS-CoV-2 Spike in convalescent individuals up to 8 months post-symptom
1465 onset. *bioRxiv* 2021.01.25.428097.
1466
- 1467 Anand, S.P., Prevost, J., Richard, J., Perreault, J., Tremblay, T., Drouin, M., Fournier, M.J., Lewin,
1468 A., Bazin, R., and Finzi, A. (2021b). High-throughput detection of antibodies targeting the SARS-
1469 CoV-2 Spike in longitudinal convalescent plasma samples. *Transfusion* 10.1111/trf.16318.
1470
- 1471 Baum, A., Ajithdoss, D., Copin, R., Zhou, A., Lanza, K., Negron, N., Ni, M., Wei, Y., Mohammadi,
1472 K., Musser, B., et al. (2020). REGN-COV2 antibodies prevent and treat SARS-CoV-2 infection in
1473 rhesus macaques and hamsters. *Science* 370, 1110-1115.
1474
- 1475 Beaudoin-Bussieres, G., Laumaea, A., Anand, S.P., Prevost, J., Gasser, R., Goyette, G.,
1476 Medjahed, H., Perreault, J., Tremblay, T., Lewin, A., et al. (2020). Decline of Humoral Responses
1477 against SARS-CoV-2 Spike in Convalescent Individuals. *mBio* 11, 10.1128/mBio.02590-02520.
1478
- 1479 Bolles, M., Deming, D., Long, K., Agnihothram, S., Whitmore, A., Ferris, M., Funkhouser, W.,
1480 Gralinski, L., Totura, A., and Heise, M. (2011). A double-inactivated severe acute respiratory
1481 syndrome coronavirus vaccine provides incomplete protection in mice and induces increased
1482 eosinophilic proinflammatory pulmonary response upon challenge. *Journal of virology* 85, 12201-
1483 12215.
1484
- 1485 Bournazos, S., DiLillo, D.J., Goff, A.J., Glass, P.J., and Ravetch, J.V. (2019). Differential
1486 requirements for FcγR engagement by protective antibodies against Ebola virus. *Proceedings of
1487 the National Academy of Sciences* 116, 20054-20062.
1488
- 1489 Bournazos, S., Klein, F., Pietzsch, J., Seaman, M.S., Nussenzweig, M.C., and Ravetch, J.V.
1490 (2014). Broadly neutralizing anti-HIV-1 antibodies require Fc effector functions for in vivo activity.
1491 *Cell* 158, 1243-1253.
1492
- 1493 Calomeni, E., Satoskar, A., Ayoub, I., Brodsky, S., Rovin, B.H., and Nadasdy, T. (2020).
1494 Multivesicular bodies mimicking SARS-CoV-2 in patients without COVID-19. *Kidney Int* 98, 233-
1495 234.
1496
- 1497 Carossino, M., Montanaro, P., O'Connell, A., Kenney, D., Gertje, H., Grosz, K.A., Kurnick, S.A.,
1498 Bosmann, M., Saeed, M., Balasuriya, U.B.R., et al. (2021). Fatal neuroinvasion of SARS-CoV-2
1499 in K18-hACE2 mice is partially dependent on hACE2 expression. *bioRxiv*,
1500 2021.2001.2013.425144.

- 1501 Chen, P., Nirula, A., Heller, B., Gottlieb, R.L., Boscia, J., Morris, J., Huhn, G., Cardona, J.,
1502 Mocherla, B., Stosor, V., *et al.* (2021). SARS-CoV-2 Neutralizing Antibody LY-CoV555 in
1503 Outpatients with Covid-19. *N Engl J Med* 384, 229-237.
- 1504
- 1505 Cohen, A.A., Gnanapragasam, P.N.P., Lee, Y.E., Hoffman, P.R., Ou, S., Kakutani, L.M., Keeffe,
1506 J.R., Wu, H.J., Howarth, M., West, A.P., *et al.* (2021). Mosaic nanoparticles elicit cross-reactive
1507 immune responses to zoonotic coronaviruses in mice. *Science* 371, 735-741.
- 1508
- 1509 Dekkers, G., Bentlage, A.E.H., Stegmann, T.C., Howie, H.L., Lissenberg-Thunnissen, S., Zimring,
1510 J., Rispens, T., and Vidarsson, G. (2017). Affinity of human IgG subclasses to mouse Fc gamma
1511 receptors. *MAbs* 9, 767-773.
- 1512
- 1513 Del Valle, D.M., Kim-Schulze, S., Huang, H.H., Beckmann, N.D., Nirenberg, S., Wang, B., Lavin,
1514 Y., Swartz, T.H., Madduri, D., Stock, A., *et al.* (2020). An inflammatory cytokine signature predicts
1515 COVID-19 severity and survival. *Nat Med* 26, 1636-1643.
- 1516
- 1517 DiLillo, D.J., Tan, G.S., Palese, P., and Ravetch, J.V. (2014). Broadly neutralizing hemagglutinin
1518 stalk-specific antibodies require FcγR interactions for protection against influenza virus *in vivo*.
1519 *Nature medicine* 20, 143-151.
- 1520
- 1521 Ding, S., Laumaea, A., Benlarbi, M., Beaudoin-Bussieres, G., Gasser, R., Medjahed, H., Pancera,
1522 M., Stamatatos, L., McGuire, A.T., Bazin, R., *et al.* (2020). Antibody Binding to SARS-CoV-2 S
1523 Glycoprotein Correlates with but Does Not Predict Neutralization. *Viruses* 12,
1524 10.1101/2020.1109.1108.287482.
- 1525
- 1526 Ellul, M.A., Benjamin, L., Singh, B., Lant, S., Michael, B.D., Easton, A., Kneen, R., Defres, S.,
1527 Sejvar, J., and Solomon, T. (2020). Neurological associations of COVID-19. *Lancet Neurol* 19,
1528 767-783.
- 1529
- 1530 Fagre, A.C., Manhard, J., Adams, R., Eckley, M., Zhan, S., Lewis, J., Rocha, S.M., Woods, C.,
1531 Kuo, K., and Liao, W. (2020). A potent SARS-CoV-2 neutralizing human monoclonal antibody that
1532 reduces viral burden and disease severity in Syrian hamsters. *Frontiers in immunology* 11,
1533 10.3389/fimmu.2020.614256.
- 1534
- 1535 Falzarano, D., Groseth, A., and Hoenen, T. (2014). Development and application of reporter-
1536 expressing mononegaviruses: current challenges and perspectives. *Antiviral Res* 103, 78-87.
- 1537
- 1538 Finzi, A., Xiang, S.H., Pacheco, B., Wang, L., Haight, J., Kassa, A., Danek, B., Pancera, M.,
1539 Kwong, P.D., and Sodroski, J. (2010). Topological layers in the HIV-1 gp120 inner domain
1540 regulate gp41 interaction and CD4-triggered conformational transitions. *Mol Cell* 37, 656-667.
- 1541
- 1542 Golden, J., Cline, C., Zeng, X., Garrison, A., Carey, B., Mucker, E., White, L., Shamblin, J.,
1543 Brocato, R., and Liu, J. (2020). Human angiotensin-converting enzyme 2 transgenic mice infected
1544 with SARS-CoV-2 develop severe and fatal respiratory disease. *JCI Insight*
1545 10.1172/jci.insight.142032.
- 1546
- 1547 Gorman, M.J., Patel, N., Guebre-Xabier, M., Zhu, A., Atyeo, C., Pullen, K.M., Loos, C., Goez-
1548 Gazi, Y., Carrion, R., Tian, J.-H., *et al.* (2021). Collaboration between the Fab and Fc contribute
1549 to maximal protection against SARS-CoV-2 in nonhuman primates following NVX-CoV2373
1550 subunit vaccine with Matrix-M™ vaccination. *bioRxiv*, 2021.2002.2005.429759.

- 1551 Graham, R.L., and Baric, R.S. (2020). SARS-CoV-2: Combating Coronavirus Emergence.
1552 *Immunity* 52, 734-736.
- 1553
- 1554 Halstead, S.B., and Katzelnick, L. (2020). COVID-19 Vaccines: Should We Fear ADE? *The*
1555 *Journal of infectious diseases* 222, 1946-1950.
- 1556
- 1557 Hansen, J., Baum, A., Pascal, K.E., Russo, V., Giordano, S., Wloga, E., Fulton, B.O., Yan, Y.,
1558 Koon, K., and Patel, K. (2020). Studies in humanized mice and convalescent humans yield a
1559 SARS-CoV-2 antibody cocktail. *Science* 369, 1010-1014.
- 1560
- 1561 Hassan, A.O., Case, J.B., Winkler, E.S., Thackray, L.B., Kafai, N.M., Bailey, A.L., McCune, B.T.,
1562 Fox, J.M., Chen, R.E., Alsoussi, W.B., *et al.* (2020). A SARS-CoV-2 Infection Model in Mice
1563 Demonstrates Protection by Neutralizing Antibodies. *Cell* 182, 744-753 e744.
- 1564
- 1565 He, W., Ladinsky, M.S., Huey-Tubman, K.E., Jensen, G.J., McIntosh, J.R., and Bjorkman, P.J.
1566 (2008). FcRn-mediated antibody transport across epithelial cells revealed by electron
1567 tomography. *Nature* 455, 542-546.
- 1568
- 1569 Hoffmann, M., Kleine-Weber, H., Schroeder, S., Kruger, N., Herrler, T., Erichsen, S., Schiergens,
1570 T.S., Herrler, G., Wu, N.H., Nitsche, A., *et al.* (2020). SARS-CoV-2 Cell Entry Depends on ACE2
1571 and TMPRSS2 and Is Blocked by a Clinically Proven Protease Inhibitor. *Cell* 181, 271-280 e278.
- 1572
- 1573 Hoffmann, M., Muller, M.A., Drexler, J.F., Glende, J., Erdt, M., Gutzkow, T., Losemann, C., Binger,
1574 T., Deng, H., Schwemmann-Wessels, C., *et al.* (2013). Differential sensitivity of bat cells to
1575 infection by enveloped RNA viruses: coronaviruses, paramyxoviruses, filoviruses, and influenza
1576 viruses. *PLoS One* 8, e72942.
- 1577
- 1578 Hofmann, H., Pyrc, K., van der Hoek, L., Geier, M., Berkhout, B., and Pohlmann, S. (2005).
1579 Human coronavirus NL63 employs the severe acute respiratory syndrome coronavirus receptor
1580 for cellular entry. *Proc Natl Acad Sci U S A* 102, 7988-7993.
- 1581
- 1582 Hsieh, C.L., Goldsmith, J.A., Schaub, J.M., DiVenere, A.M., Kuo, H.C., Javanmardi, K., Le, K.C.,
1583 Wrapp, D., Lee, A.G., Liu, Y., *et al.* (2020). Structure-based design of prefusion-stabilized SARS-
1584 CoV-2 spikes. *Science* 369, 1501-1505.
- 1585
- 1586 Iwasaki, A., and Yang, Y. (2020). The potential danger of suboptimal antibody responses in
1587 COVID-19. *Nat Rev Immunol* 20, 339-341.
- 1588
- 1589 Johansen, M.D., Irving, A., Montagutelli, X., Tate, M.D., Rudloff, I., Nold, M.F., Hansbro, N.G.,
1590 Kim, R.Y., Donovan, C., Liu, G., *et al.* (2020). Animal and translational models of SARS-CoV-2
1591 infection and COVID-19. *Mucosal Immunol* 13, 877-891.
- 1592
- 1593 Juette, M.F., Terry, D.S., Wasserman, M.R., Altman, R.B., Zhou, Z., Zhao, H., and Blanchard,
1594 S.C. (2016). Single-molecule imaging of non-equilibrium molecular ensembles on the millisecond
1595 timescale. *Nat Methods* 13, 341-344.
- 1596
- 1597 Ke, Z., Oton, J., Qu, K., Cortese, M., Zila, V., McKeane, L., Nakane, T., Zivanov, J., Neufeldt,
1598 C.J., Cerikan, B., *et al.* (2020). Structures and distributions of SARS-CoV-2 spike proteins on
1599 intact virions. *Nature* 588, 498-502.
- 1600

- 1601 Klasse, P.J., and Moore, J.P. (2020). Antibodies to SARS-CoV-2 and their potential for
1602 therapeutic passive immunization. *eLife* 9, 10.7554/eLife.57877.
1603
- 1604 Klein, S., Cortese, M., Winter, S.L., Wachsmuth-Melm, M., Neufeldt, C.J., Cerikan, B., Stanifer,
1605 M.L., Boulant, S., Bartenschlager, R., and Chlonda, P. (2020). SARS-CoV-2 structure and
1606 replication characterized by *in situ* cryo-electron tomography. *Nat Commun* 11, 5885.
1607 Ladinsky, M.S., Huey-Tubman, K.E., and Bjorkman, P.J. (2012). Electron tomography of late
1608 stages of FcRn-mediated antibody transcytosis in neonatal rat small intestine. *Mol Biol Cell* 23,
1609 2537-2545.
1610
- 1611 Leist, S.R., Dinnon, K.H., 3rd, Schafer, A., Tse, L.V., Okuda, K., Hou, Y.J., West, A., Edwards,
1612 C.E., Sanders, W., Fritch, E.J., *et al.* (2020a). A Mouse-Adapted SARS-CoV-2 Induces Acute
1613 Lung Injury and Mortality in Standard Laboratory Mice. *Cell* 183, 1070-1085 e1012.
1614
- 1615 Leist, S.R., Schäfer, A., and Martinez, D.R. (2020b). Cell and animal models of SARS-CoV-2
1616 pathogenesis and immunity. *Disease Models & Mechanisms* 13, dmm046581.
1617
- 1618 Li, D., Edwards, R.J., Manne, K., Martinez, D.R., Schäfer, A., Alam, S.M., Wiehe, K., Lu, X., Parks,
1619 R., Sutherland, L.L., *et al.* (2021). The functions of SARS-CoV-2 neutralizing and infection-
1620 enhancing antibodies *in vitro* and *in vivo* in mice and nonhuman primates. *bioRxiv*,
1621 2020.2012.2031.424729.
1622
- 1623 Li, W., Chen, C., Drelich, A., Martinez, D.R., Gralinski, L.E., Sun, Z., Schafer, A., Kulkarni, S.S.,
1624 Liu, X., Leist, S.R., *et al.* (2020). Rapid identification of a human antibody with high prophylactic
1625 and therapeutic efficacy in three animal models of SARS-CoV-2 infection. *Proc Natl Acad Sci U
1626 S A* 117, 29832-29838.
1627
- 1628 Liu, L., Wang, P., Nair, M.S., Yu, J., Rapp, M., Wang, Q., Luo, Y., Chan, J.F., Sahi, V., Figueroa,
1629 A., *et al.* (2020). Potent neutralizing antibodies against multiple epitopes on SARS-CoV-2 spike.
1630 *Nature* 584, 450-456.
1631
- 1632 Liu, Z., Pan, Q., Ding, S., Qian, J., Xu, F., Zhou, J., Cen, S., Guo, F., and Liang, C. (2013). The
1633 interferon-inducible MxB protein inhibits HIV-1 infection. *Cell Host Microbe* 14, 398-410.
1634 Lu, L.L., Suscovich, T.J., Fortune, S.M., and Alter, G. (2018). Beyond binding: antibody effector
1635 functions in infectious diseases. *Nature Reviews Immunology* 18, 46.
1636
- 1637 Lu, M., Ma, X., Castillo-Menendez, L.R., Gorman, J., Alsahafi, N., Ermel, U., Terry, D.S.,
1638 Chambers, M., Peng, D., Zhang, B., *et al.* (2019). Associating HIV-1 envelope glycoprotein
1639 structures with states on the virus observed by smFRET. *Nature* 568, 415-419.
1640
- 1641 Lu, M., Uchil, P.D., Li, W., Zheng, D., Terry, D.S., Gorman, J., Shi, W., Zhang, B., Zhou, T., Ding,
1642 S., *et al.* (2020). Real-Time Conformational Dynamics of SARS-CoV-2 Spikes on Virus Particles.
1643 *Cell Host Microbe* 28, 880-891 e888.
1644
- 1645 Mack, M., Cihak, J., Simonis, C., Luckow, B., Proudfoot, A.E., Plachý, J.í., Brühl, H., Frink, M.,
1646 Anders, H.-J., and Vielhauer, V. (2001). Expression and characterization of the chemokine
1647 receptors CCR2 and CCR5 in mice. *The Journal of Immunology* 166, 4697-4704.
1648
- 1649 Mastronarde, D.N. (2005). Automated electron microscope tomography using robust prediction
1650 of specimen movements. *J Struct Biol* 152, 36-51.

- 1651 Mastronarde, D.N. (2008). Correction for non-perpendicularity of beam and tilt axis in tomographic
1652 reconstructions with the IMOD package. *J Microsc* 230, 212-217.
- 1653
- 1654 Mastronarde, D.N., and Held, S.R. (2017). Automated tilt series alignment and tomographic
1655 reconstruction in IMOD. *J Struct Biol* 197, 102-113.
- 1656
- 1657 McCray, P.B., Pewe, L., Wohlford-Lenane, C., Hickey, M., Manzel, L., Shi, L., Netland, J., Jia,
1658 H.P., Halabi, C., and Sigmund, C.D. (2007). Lethal infection of K18-hACE2 mice infected with
1659 severe acute respiratory syndrome coronavirus. *Journal of virology* 81, 813-821.
- 1660
- 1661 Munro, J.B., Gorman, J., Ma, X., Zhou, Z., Arthos, J., Burton, D.R., Koff, W.C., Courter, J.R.,
1662 Smith, A.B., 3rd, Kwong, P.D., et al. (2014). Conformational dynamics of single HIV-1 envelope
1663 trimers on the surface of native virions. *Science* 346, 759-763.
- 1664
- 1665 Noy-Porat, T., Mechaly, A., Levy, Y., Makdasi, E., Alcalay, R., Gur, D., Aftalion, M., Falach, R.,
1666 Ben-Arye, S.L., Lazar, S., et al. (2021). Therapeutic antibodies, targeting the SARS-CoV-2 spike
1667 N-terminal domain, protect lethally infected K18-hACE2 mice. *bioRxiv*, 2021.2002.428995.
- 1668
- 1669 Park, J.E., Li, K., Barlan, A., Fehr, A.R., Perlman, S., McCray, P.B., Jr., and Gallagher, T. (2016).
1670 Proteolytic processing of Middle East respiratory syndrome coronavirus spikes expands virus
1671 tropism. *Proc Natl Acad Sci U S A* 113, 12262-12267.
- 1672
- 1673 Prevost, J., Gasser, R., Beaudoin-Bussieres, G., Richard, J., Duerr, R., Laumaea, A., Anand,
1674 S.P., Goyette, G., Benlarbi, M., Ding, S., et al. (2020). Cross-Sectional Evaluation of Humoral
1675 Responses against SARS-CoV-2 Spike. *Cell Rep Med* 1, 100126.
- 1676
- 1677 Rogers, T.F., Zhao, F., Huang, D., Beutler, N., Burns, A., He, W.T., Limbo, O., Smith, C., Song,
1678 G., Woehl, J., et al. (2020). Isolation of potent SARS-CoV-2 neutralizing antibodies and protection
1679 from disease in a small animal model. *Science* 369, 956-963.
- 1680
- 1681 Ruckwardt, T.J., Morabito, K.M., and Graham, B.S. (2019). Immunological lessons from
1682 respiratory syncytial virus vaccine development. *Immunity* 51, 429-442.
- 1683
- 1684 Saunders, K.O. (2019). Conceptual Approaches to Modulating Antibody Effector Functions and
1685 Circulation Half-Life. *Front Immunol* 10, 1296.
- 1686
- 1687 Schafer, A., Muecksch, F., Lorenzi, J.C.C., Leist, S.R., Cipolla, M., Bournazos, S., Schmidt, F.,
1688 Maison, R.M., Gazumyan, A., Martinez, D.R., et al. (2021). Antibody potency, effector function,
1689 and combinations in protection and therapy for SARS-CoV-2 infection in vivo. *J Exp Med* 218,
1690 10.1084/jem.20201993.
- 1691
- 1692 Shi, P.Y., Plante, J., Liu, Y., Liu, J., Xia, H., Johnson, B., Lokugamage, K., Zhang, X., Muruato,
1693 A., Zou, J., et al. (2020a). Spike mutation D614G alters SARS-CoV-2 fitness and neutralization
1694 susceptibility. *Res Sq*, 10.21203/rs.21203.rs-70482/v21201.
- 1695
- 1696 Shi, R., Shan, C., Duan, X., Chen, Z., Liu, P., Song, J., Song, T., Bi, X., Han, C., and Wu, L.
1697 (2020b). A human neutralizing antibody targets the receptor-binding site of SARS-CoV-2. *Nature*
1698 584, 120-124.
- 1699

- 1700 Silvas, J., Morales-Vasquez, D., Park, J.-G., Chiem, K., Torrelles, J.B., Platt, R.N., Anderson, T.,
1701 Ye, C., and Martinez-Sobrido, L. (2021). Contribution of SARS-CoV-2 accessory proteins to viral
1702 pathogenicity in K18 hACE2 transgenic mice. bioRxiv, 2021.2003.2009.434696.
1703
- 1704 Smith, P., DiLillo, D.J., Bournazos, S., Li, F., and Ravetch, J.V. (2012). Mouse model
1705 recapitulating human Fcγ receptor structural and functional diversity. Proceedings of the National
1706 Academy of Sciences 109, 6181-6186.
1707
- 1708 Stamatatos, L., Czartoski, J., Wan, Y.-H., Homad, L.J., Rubin, V., Glantz, H., Neradilek, M.,
1709 Seydoux, E., Jennewein, M.F., MacCamay, A.J., et al. (2021). Antibodies elicited by SARS-CoV-2
1710 infection and boosted by vaccination neutralize an emerging variant and SARS-CoV-1. medRxiv,
1711 2021.2002.2005.21251182.
1712
- 1713 ter Meulen, J., van den Brink, E.N., Poon, L.L., Marissen, W.E., Leung, C.S., Cox, F., Cheung,
1714 C.Y., Bakker, A.Q., Bogaards, J.A., van Deventer, E., et al. (2006). Human monoclonal antibody
1715 combination against SARS coronavirus: synergy and coverage of escape mutants. PLoS Med 3,
1716 e237.
1717
- 1718 Tortorici, M.A., Beltramello, M., Lempp, F.A., Pinto, D., Dang, H.V., Rosen, L.E., McCallum, M.,
1719 Bowen, J., Minola, A., Jaconi, S., et al. (2020). Ultrapotent human antibodies protect against
1720 SARS-CoV-2 challenge via multiple mechanisms. Science 370, 950-957.
1721
- 1722 Turonova, B., Sikora, M., Schurmann, C., Hagen, W.J.H., Welsch, S., Blanc, F.E.C., von Bulow,
1723 S., Gecht, M., Bagola, K., Horner, C., et al. (2020). In situ structural analysis of SARS-CoV-2
1724 spike reveals flexibility mediated by three hinges. Science 370, 203-208.
1725
- 1726 Ventura, J.D., Beloór, J., Allen, E., Zhang, T., Haugh, K.A., Uchil, P.D., Ochsenbauer, C., Kieffer,
1727 C., Kumar, P., Hope, T.J., et al. (2019). Longitudinal bioluminescent imaging of HIV-1 infection
1728 during antiretroviral therapy and treatment interruption in humanized mice. PLoS Pathog 15,
1729 e1008161.
1730
- 1731 Voss, W.N., Hou, Y.J., Johnson, N.V., Kim, J.E., Delidakis, G., Horton, A.P., Bartzoka, F., Paresi,
1732 C.J., Tanno, Y., Abbasi, S.A., et al. (2020). Prevalent, protective, and convergent IgG recognition
1733 of SARS-CoV-2 non-RBD spike epitopes in COVID-19 convalescent plasma. bioRxiv,
1734 10.1101/2020.1112.1120.423708.
1735
- 1736 Weinreich, D.M., Sivapalasingam, S., Norton, T., Ali, S., Gao, H., Bhore, R., Musser, B.J., Soo,
1737 Y., Rofail, D., Im, J., et al. (2021). REGN-COV2, a Neutralizing Antibody Cocktail, in Outpatients
1738 with Covid-19. N Engl J Med 384, 238-251.
1739
- 1740 Winkler, E.S., Bailey, A.L., Kafai, N.M., Nair, S., McCune, B.T., Yu, J., Fox, J.M., Chen, R.E.,
1741 Earnest, J.T., and Keeler, S.P. (2020). SARS-CoV-2 infection of human ACE2-transgenic mice
1742 causes severe lung inflammation and impaired function. Nature immunology 21, 1327-1335.
1743
- 1744 Winkler, E.S., Gilchuk, P., Yu, J., Bailey, A.L., Chen, R.E., Chong, Z., Zost, S.J., Jang, H., Huang,
1745 Y., Allen, J.D., et al. (2021). Human neutralizing antibodies against SARS-CoV-2 require intact
1746 Fc effector functions for optimal therapeutic protection. Cell, 10.1016/j.cell.2021.1002.1026.
1747
- 1748 Xie, X., Muruato, A., Lokugamage, K.G., Narayanan, K., Zhang, X., Zou, J., Liu, J., Schindewolf,
1749 C., Bopp, N.E., Aguilar, P.V., et al. (2020a). An Infectious cDNA Clone of SARS-CoV-2. Cell Host
1750 Microbe 27, 841-848 e843.

- 1751
1752 Xie, X., Muruato, A.E., Zhang, X., Lokugamage, K.G., Fontes-Garfias, C.R., Zou, J., Liu, J., Ren,
1753 P., Balakrishnan, M., Cihlar, T., *et al.* (2020b). A nanoluciferase SARS-CoV-2 for rapid
1754 neutralization testing and screening of anti-infective drugs for COVID-19. *Nat Commun* 11, 5214.
1755
1756 Yao, H., Song, Y., Chen, Y., Wu, N., Xu, J., Sun, C., Zhang, J., Weng, T., Zhang, Z., Wu, Z., *et*
1757 *al.* (2020). Molecular Architecture of the SARS-CoV-2 Virus. *Cell* 183, 730-738 e713.
1758
1759 Zhang, L., Jackson, C.B., Mou, H., Ojha, A., Peng, H., Quinlan, B.D., Rangarajan, E.S., Pan, A.,
1760 Vanderheiden, A., Suthar, M.S., *et al.* (2020). SARS-CoV-2 spike-protein D614G mutation
1761 increases virion spike density and infectivity. *Nat Commun* 11, 10.1038/s41467-41020-19808-
1762 41464.
1763
1764 Zost, S.J., Gilchuk, P., Case, J.B., Binshtein, E., Chen, R.E., Nkolola, J.P., Schäfer, A., Reidy,
1765 J.X., Trivette, A., and Nargi, R.S. (2020a). Potently neutralizing and protective human antibodies
1766 against SARS-CoV-2. *Nature* 584, 443-449.
1767
1768 Zost, S.J., Gilchuk, P., Chen, R.E., Case, J.B., Reidy, J.X., Trivette, A., Nargi, R.S., Sutton, R.E.,
1769 Suryadevara, N., and Chen, E.C. (2020b). Rapid isolation and profiling of a diverse panel of
1770 human monoclonal antibodies targeting the SARS-CoV-2 spike protein. *Nature medicine* 26,
1771 1422-1427.

Figure 1

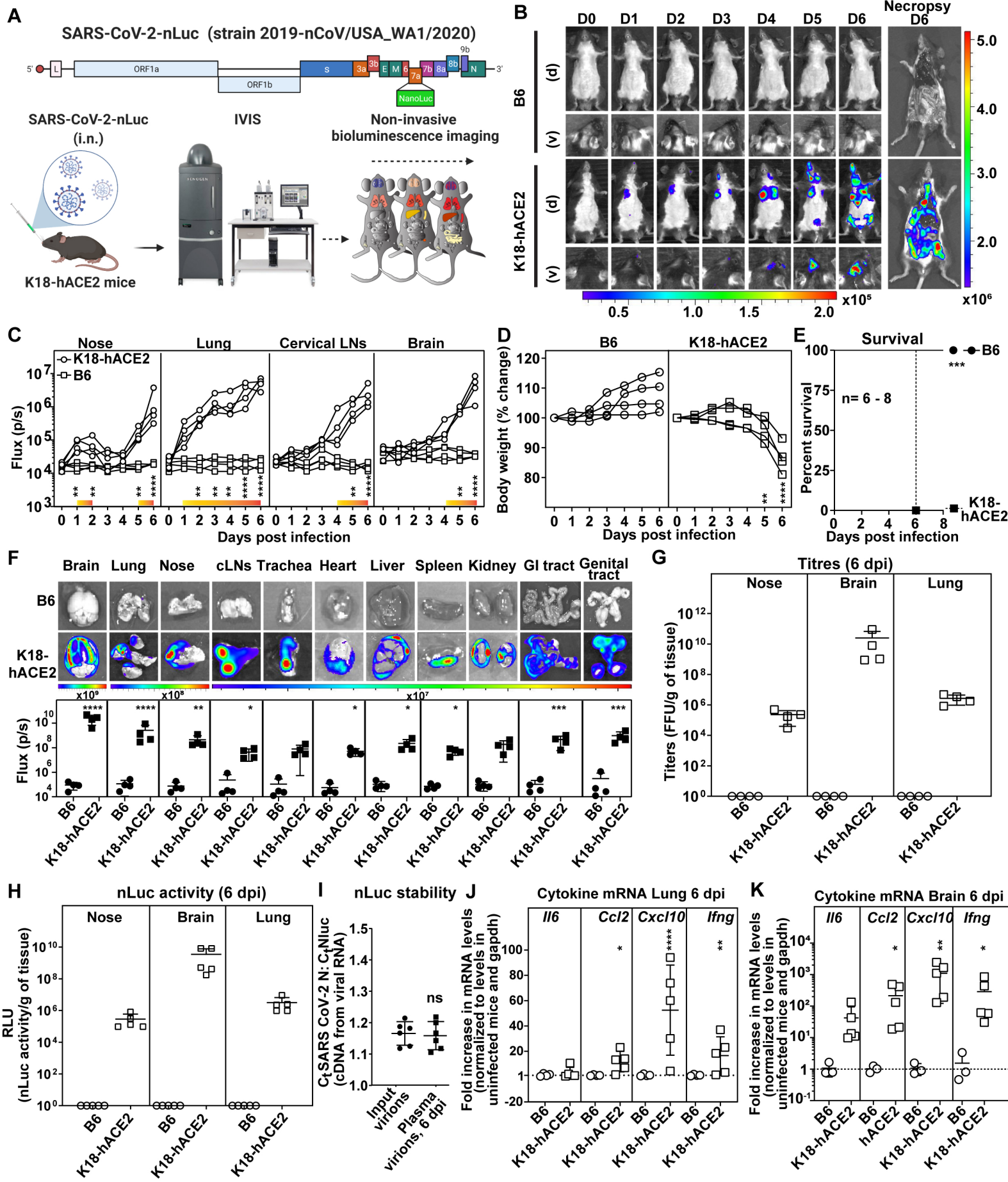
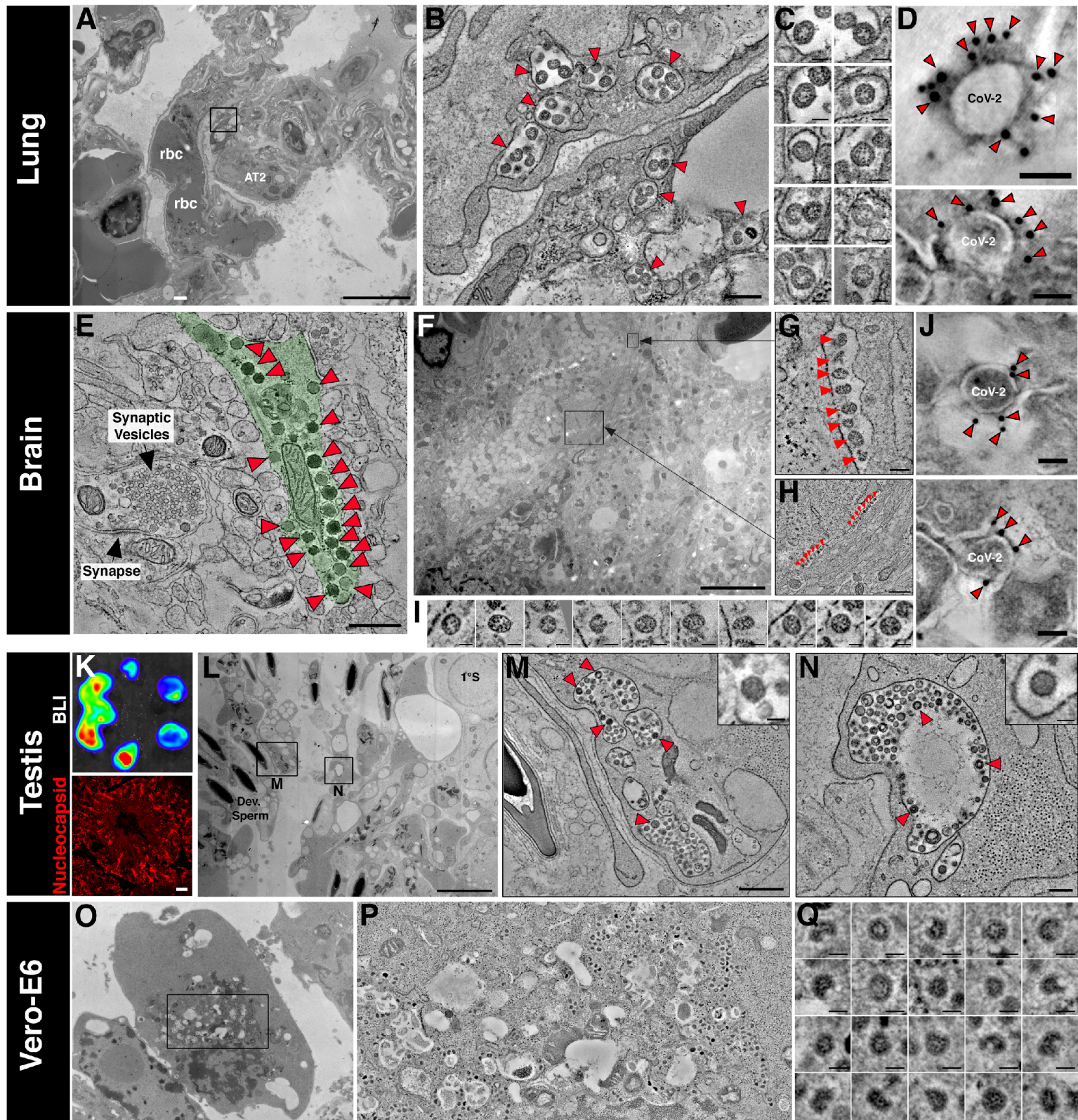


Figure 2



A: 5 μm; B: 0.2 μm; C,D: 0.05 μm; E: 0.5 μm; F: 5 μm; G: 0.1 μm; I,J: 0.05 μm; K: 20 μm; L: 5 μm; K inset: 0.05 μm; N: 0.05 μm; N inset: 0.05 μm; O: 2 μm; P: 0.5 μm; Q: 0.05 μm

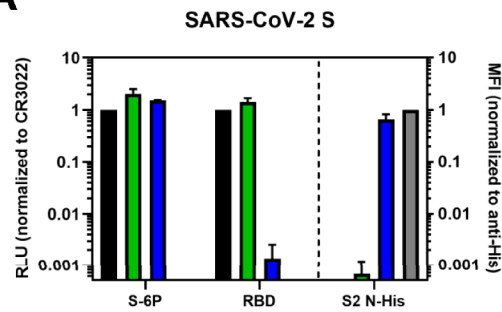
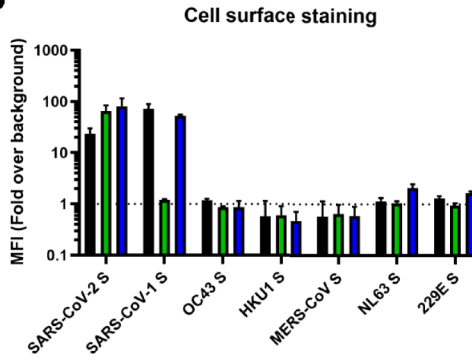
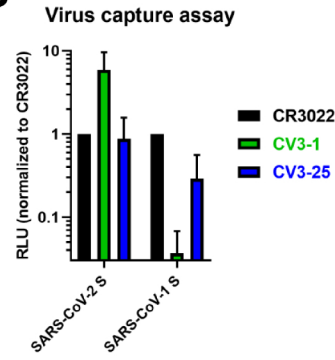
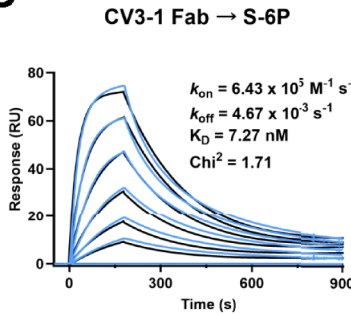
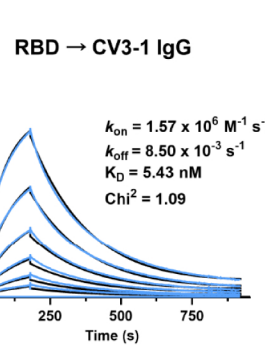
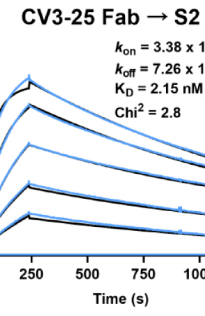
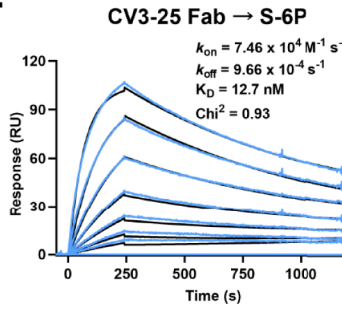
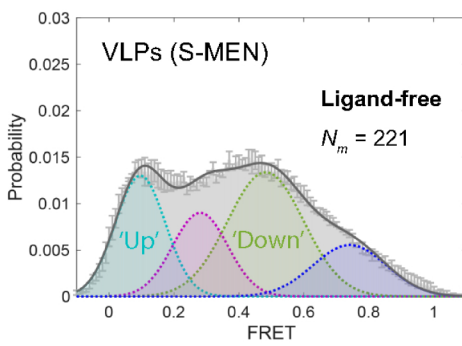
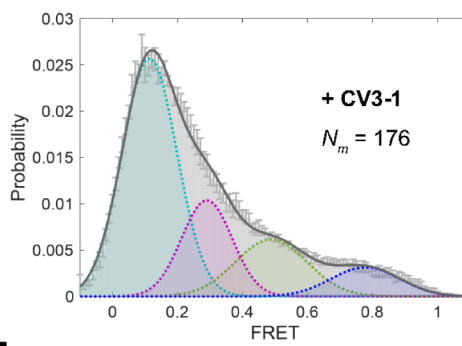
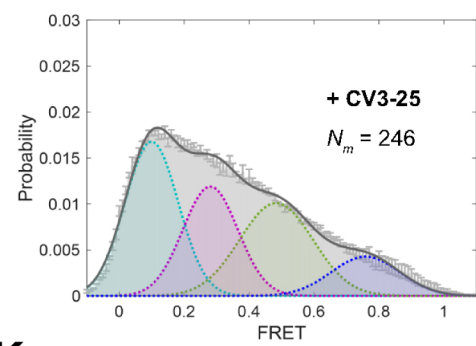
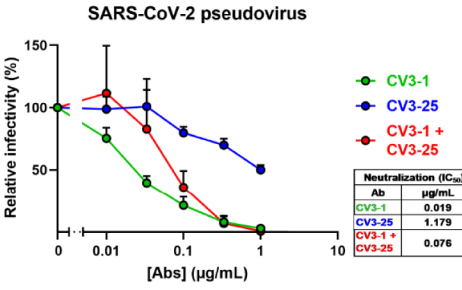
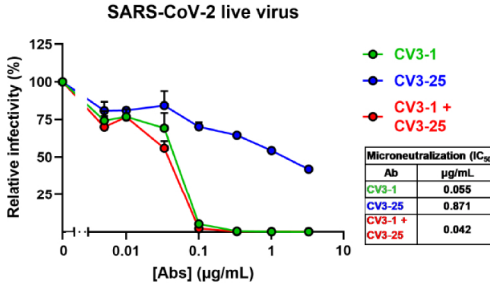
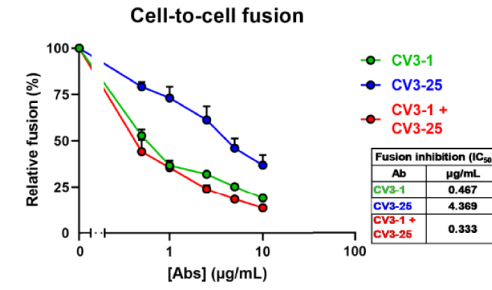
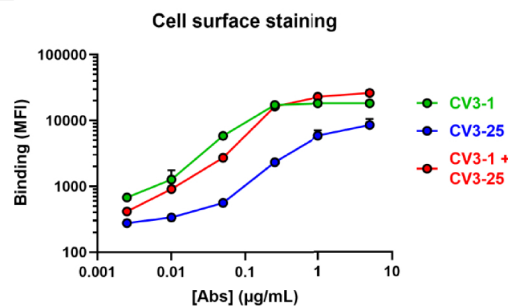
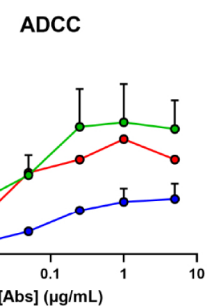
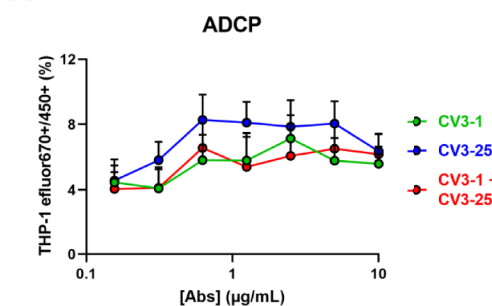
Figure 3**A****B****C****D****RBD → CV3-1 IgG****E****F****G****H****I****J****K****L****M****N**

Figure 4

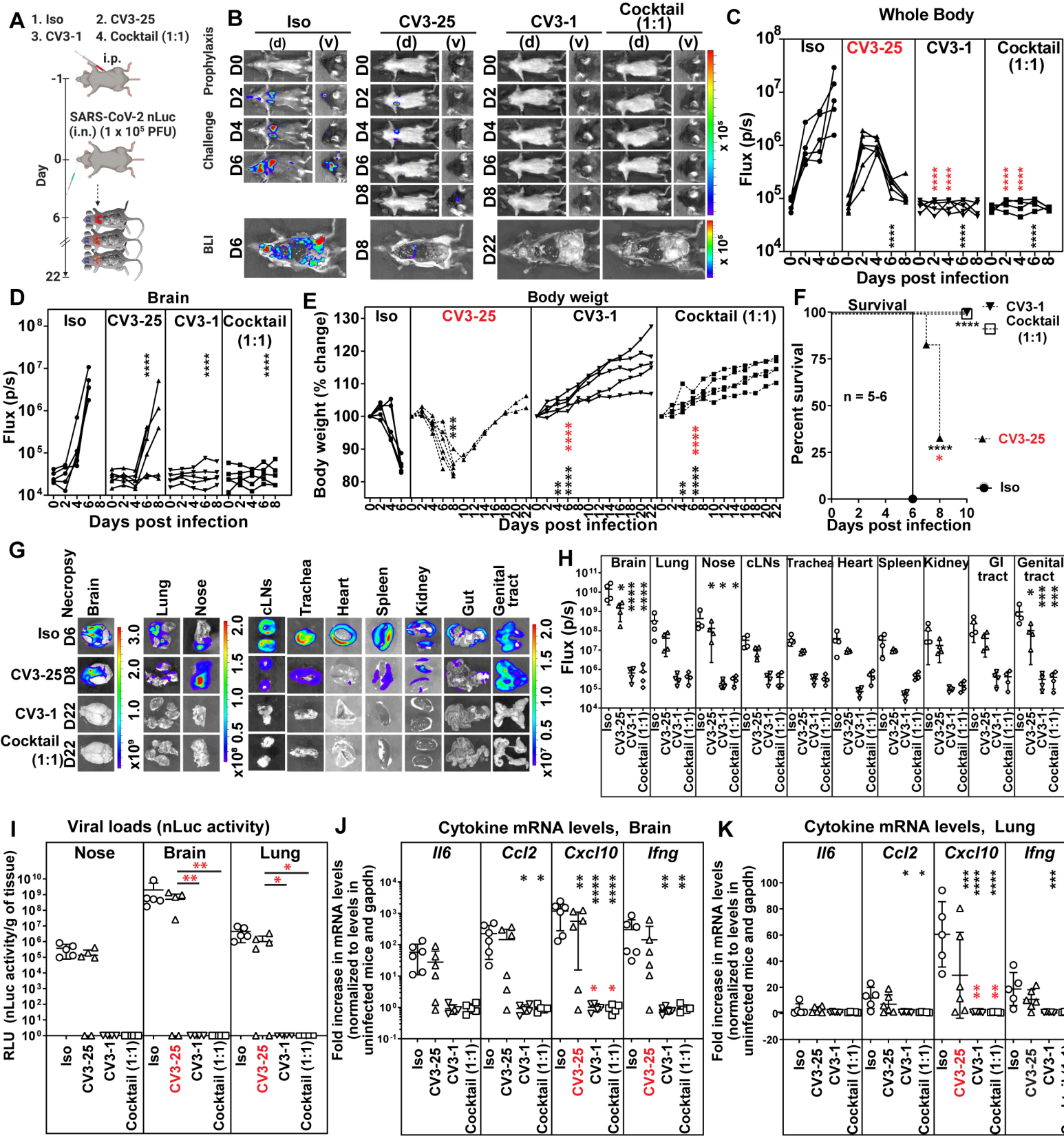


Figure 5

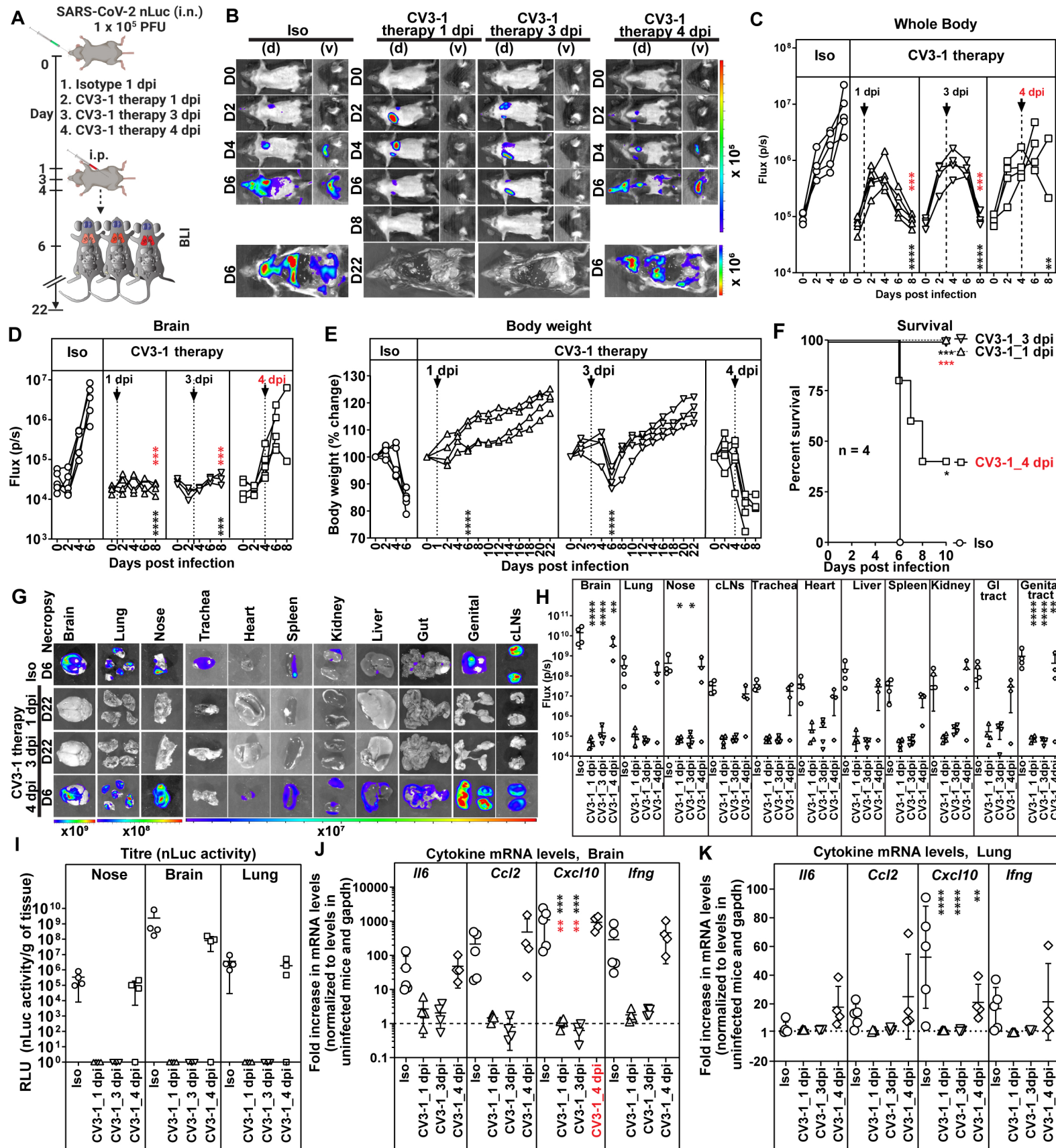


Figure 6

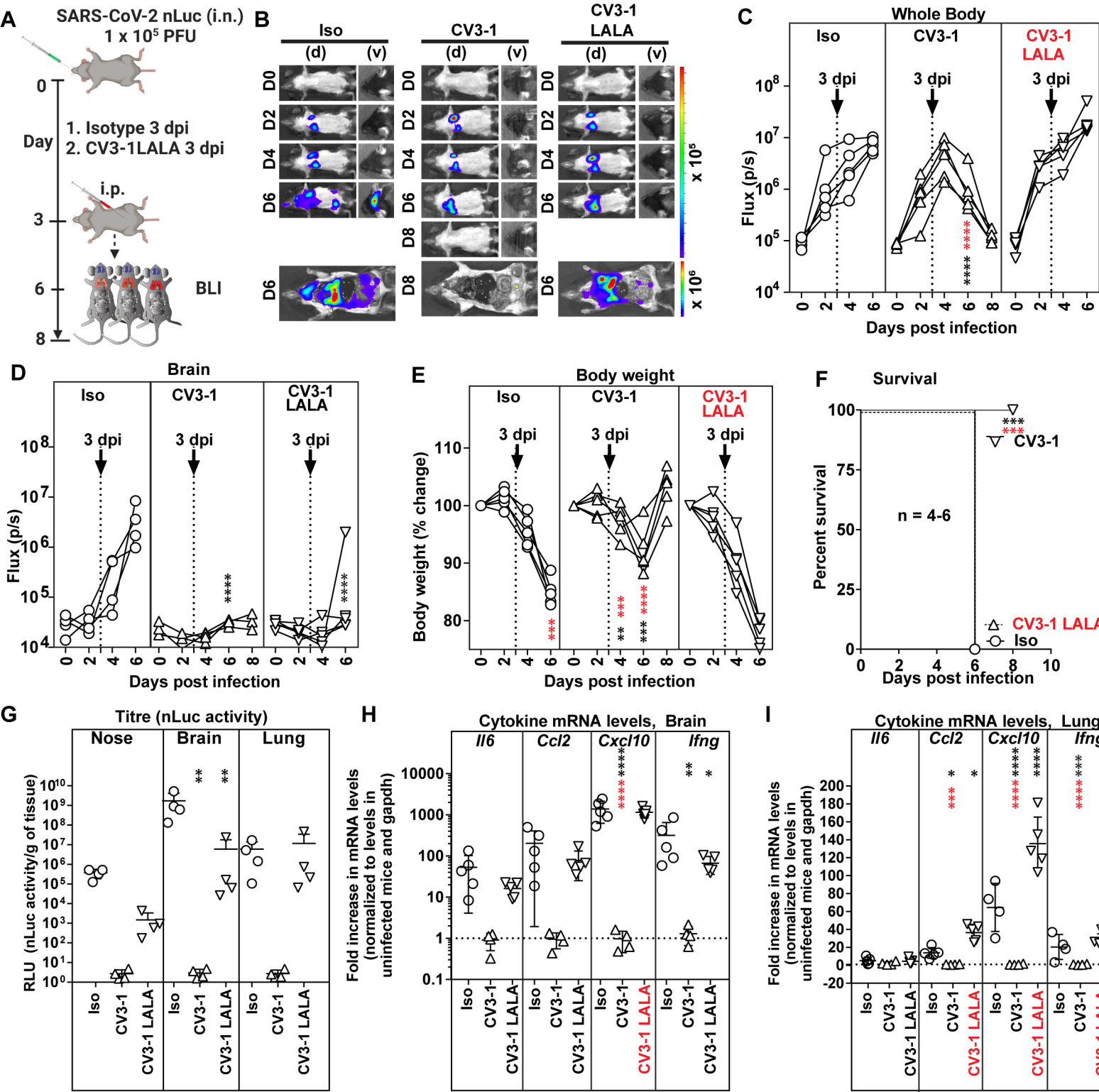


Figure 7

